Hot Forging Options for Thick Castings

July 2022

JI Royer
S Shahrezaei
A Soulami
KP Brooks
MT Athon
ZF Huber

Mark Rhodes
RJ Seffens
JB Lang
VV Joshi
AL Schemer-Kohrn

DISCLAIMER

This report was prepared as an account of work sponsored by an agency of the United States Government. Neither the United States Government nor any agency thereof, nor Battelle Memorial Institute, nor any of their employees, makes **any warranty, express or implied, or assumes any legal liability or responsibility for the accuracy, completeness, or usefulness of any information, apparatus, product, or process disclosed, or represents that its use would not infringe privately owned rights**. Reference herein to any specific commercial product, process, or service by trade name, trademark, manufacturer, or otherwise does not necessarily constitute or imply its endorsement, recommendation, or favoring by the United States Government or any agency thereof, or Battelle Memorial Institute. The views and opinions of authors expressed herein do not necessarily state or reflect those of the United States Government or any agency thereof.

PACIFIC NORTHWEST NATIONAL LABORATORY
operated by
BATTELLE
for the
UNITED STATES DEPARTMENT OF ENERGY
under Contract DE-AC05-76RL01830

Printed in the United States of America

Available to DOE and DOE contractors from
the Office of Scientific and Technical Information,
P.O. Box 62, Oak Ridge, TN 37831-0062
www.osti.gov
ph: (865) 576-8401
fox: (865) 576-5728
email: reports@osti.gov

Available to the public from the National Technical Information Service
5301 Shawnee Rd., Alexandria, VA 22312
ph: (800) 553-NTIS (6847)
or (703) 605-6000
email: info@ntis.gov
Online ordering: http://www.ntis.gov

Hot Forging Options for Thick Castings

July 2022

JI Royer
S Shahrezaei
A Soulami
KP Brooks
MT Athon
ZF Huber

Mark Rhodes
RJ Seffens
JB Lang
VV Joshi
AL Schemer-Kohrn

Pacific Northwest National Laboratory
Richland, Washington 99354

Summary

Uranium alloyed with 10 wt% molybdenum (U-10Mo) is a monolithic nuclear fuel relevant to the National Nuclear Security Administration's nonproliferation efforts. Research has been underway to optimize processing techniques for the U-10Mo fuel. This study investigated the use of hot compression or "hot forging" on a thick (~1") cast and homogenized U-10Mo plate before standard hot and cold rolling procedures. After plates were cast and homogenized, six samples were cut and forged at 700°C at a strain rate of either $0.10\ s^{-1}$ or $0.01\ s^{-1}$ at six levels of reduction. After forging, all samples underwent hot and cold rolling followed by annealing to achieve a final foil thickness of about 0.0085". Samples were taken at each stage of the casting and thermomechanical processing to assess the microstructural evolution. Chemical composition, microstructure, and uranium carbide morphology are presented and assessed in this study. Upon hot forging, dislocations accumulate along the grain boundaries, which serve as nucleation sites for randomly oriented, strain-free grains during subsequent annealing steps. Hot forging and subsequent annealing produced very heterogeneous grain sizes. However, no molybdenum segregation was observed after forging. No obvious trend was observed between forging conditions (strain rate and reduction percentage) and the microstructure after final thermomechanical processing. Upon hot rolling to 0.04" and annealing (700°C for 45 min), the average grain diameters from OM was 17 ± 2 μm across the six different forged samples. The subsequent cold rolling to 0.0085" and then annealing (700°C for 45 min) resulted in an average of 13 ± 2 μm between the six samples. Thus, the starting, as-forged microstructure did not appear to significantly influence the final microstructure of the cold-rolled foil. These results will help with understanding and expanding hot working capabilities for thicker U-10Mo castings. They also provide useful information on the effects of hot forging and its potential use to minimize defects that can arise during subsequent hot and cold rolling procedures.

Acknowledgments

Acronyms and Abbreviations

BSE	backscattered electron
C	carbon
EBSD	electron backscatter diffraction
EDS	energy-dispersive x-ray spectroscopy
GOS	grain orientation spread
HIP	hot isostatic pressing
ICP-OES	inductively coupled plasma–optical emission spectrometry
Mo	molybdenum
NA	not applicable
OM	optical microscopy
PNNL	Pacific Northwest National Laboratory
ppm	part(s) per million
PSN	particle stimulated nucleation
SD	standard deviation
SEM	scanning electron microscopy
U-10Mo	uranium alloyed with 10 weight percent molybdenum
UC	uranium carbide
VIM	vacuum induction melter
Zr	zirconium

Contents

Figures

Tables

1.0 Introduction

Uranium alloyed with 10 wt% molybdenum (U-10Mo) has been identified as a potential replacement for highly enriched uranium fuel as part of the United States High Performance Research Reactor Conversion Program. Converting research reactors from highly enriched uranium fuels to low-enriched uranium fuels is part of an ongoing effort to reduce the risk of nuclear proliferation. Fabricating the U-10Mo fuel involves casting, homogenization, sectioning into coupons, hot roll bonding with zirconium (Zr), cold rolling, annealing, and final bonding of a 6061 aluminum cladding via hot isostatic pressing (HIP). Research is ongoing on methods to improve the processing parameters of the fuel. It is vital to optimize thermomechanical processing to yield good fuel quality and cost effective manufacturing (Hu et al. 2018; Joshi, Nyberg, Lavender, Paxton, Garmestani, et al. 2015; W. E. Frazier et al. 2019; William E. Frazier et al. 2018; Senor and Burkes 2014).

It has been observed that after the Zr bonding and hot rolling procedure, the foil has an uneven, "orange peel" surface texture. During the Zr bonding process, 0.010" (0.25 mm) thick Zr foils are placed on either side of the homogenized U-10Mo coupon, assembled into a steel can, and welded shut. After hot rolling, the coupon is removed from the can; then annealing and subsequent cold rolling, annealing, and HIP processing are performed. The purpose of the Zr co-rolling is to add a diffusion barrier between the U-10Mo and the aluminum cladding, limiting interaction between the fuel meat and cladding (Senor and Burkes 2014; Wachs, Clark, and Dunavant 2008; Sease, Primm III, and Miller 2007; Hu et al. 2018; Pacheco et al. 2017; Jue et al. 2015). However, the rough, orange peel surface appearance can cause issues during subsequent processing and final fuel performance. Orange peel is a defect associated with metal after forming operations, particularly with sheet metals after hot-roll bonding. The defect is caused by individual grains deforming to varying degrees, resulting in thickness variation among them and a surface resembling an orange peel. The orange peel surface defect is exacerbated with larger grains and greater deformation. A more refined grain size may prevent orange peel and reduce the thickness variation. Hence, ease of forming, (associated with larger-grained material) and avoiding the orange peel texture (associated with smaller grains) must be balanced (Pacheco et al. 2017; Hosford 2010; Llewellyn 1998; Llewellyn and Hudd 1998; Al-Qureshi, Klein, and Fredel 2005; Yamaguchi and Mellor 1976; Lee et al. 1998).

One method proposed for avoiding orange peel is to start with a thicker casting (~1" thick) and then apply aggressive thermomechanical processing, such as hot forging and rolling, to reduce the starting grain size before the standard hot and cold rolling, the goal being uniform U-10Mo thickness and a smooth U-10Mo/Zr interface after co-rolling. Implementation of forging could also potentially reduce the need for other thermomechanical processing, and thereby streamline fabrication.

In addition to allowing for more aggressive thermomechanical processing to help refine grains, using thicker castings can also help optimize cost and reduce waste. Thicker castings provide more bulk material with uniform microstructure to minimize defects (Huber, McCoy, et al. 2021). However, implementing the use of thicker castings also requires development of forming mechanisms, such as hot forging, to reduce the starting thickness to meet the requirements for the traditional Zr interlayer co-rolling step.

The purpose of this study is to investigate the effect of hot forging on subsequent thermomechanical processing of U-10Mo. This includes homogenization, hot rolling, cold rolling,

and annealing procedures. The microstructural evolution throughout processing will be analyzed and used to inform the fuel fabricator, for future operations.

2.0   Materials and Methods

This section describes plate fabrication, thermomechanical processing, bulk chemistry, sample preparation, microscopy techniques, and analysis methods. After each material processing step, samples were cut for metallography and chemical analysis.

2.1   Plate Fabrication

The U-10Mo casting used in this study (Thick Casting 5) was manufactured at Pacific Northwest National Laboratory's (PNNL's) Radiochemical Processing Laboratory using a commercial tilt-pour vacuum induction melter (VIM; Indutherm VTC 200Ti). Approximately 1434 g of depleted-uranium feedstock from Zero Power Physics Reactor brick and 159 g of 0.04" thick molybdenum (Mo) wire from Elmet Technologies were used for the casting (1592.83 g total). The carbon (C) concentration of the depleted-uranium feedstock was 130 ± 8 ppm, and the molybdenum wire feedstock was 99.95% molybdenum with a carbon concentration of 35 ± 9 ppm (Huber, McCoy, et al. 2021). This thick casting was cast in a 3.56" deep rectangular graphite mold with a 1" by 2" cross section. The crucible used was magnesia-stabilized zirconia (ZrO_2) from Zircoa Inc. Both the crucible and mold were cleaned with ethanol and coated with aerosol yttria (Y_2O_3) paint and then dried in a furnace at 100°C after each of three coats prior to casting. The wash and coating are performed to limit interactions of molten uranium (U) with the graphite during casting. To volatize any impurities, the VIM was evacuated and heated to 400–600°C for approximately two hours prior to use. Once the mold and crucible were set up, the VIM chamber was evacuated using roughing and turbo vacuum pumps and backfilled with argon gas three times to promote a clean casting atmosphere. The casting was made using 9 kW power and held for 15 minutes at a superheat temperature of approximately 1400°C prior to pouring. Upon pouring, the mold temperature was 458°C. The final cast plate, shown in Figure 2-1, weighed 1545 g and was approximately 3.07" long, 1.96" wide, and 0.984" thick (78 × 25 × 50 mm). A typical U-Mo plate produced at the Radiochemical Processing Laboratory is approximately 0.2" thick, which is why this plate is referred to as a "thick" casting (Huber, McCoy, et al. 2021; Huber, Athon, et al. 2021).

Figure 2-1. Thick Plate 5 casting

2.2   Thermomechanical Processing

Before metal forming, six samples approximately 0.3" x 0.3" x 1" were cut from the as-cast plate. Each piece was wrapped in zirconium (Zr) foil to reduce oxidation and then homogenized in argon for 144 hours at 900°C inside an MTI Corporation Model VBF-1200X-H8 furnace. This created a uniform and mostly equiaxed microstructure with no molybdenum segregation before hot forging.

Hot hydraulic forging was conducted at 700°C using an Instron Model 8801 Universal Testing System and a 22,500 lb (100 kN) load cell from the PNNL Physical Sciences Facility. Figure 2-2 shows the test frame and forging setup used. Samples were wrapped in Zr foil before forging to limit oxidation. The hot forging was then performed on six homogenized samples at a strain rate of either 0.01 s^{-1} or 0.1 s^{-1}. This resulted in six samples, each with either 79%, 64%, 38%, 41%, 56.1%, or 55.8% reduction, as outlined in Table 2.1. A stress-strain curve for the six samples during forging can be found in the appendix as Figure A.1.
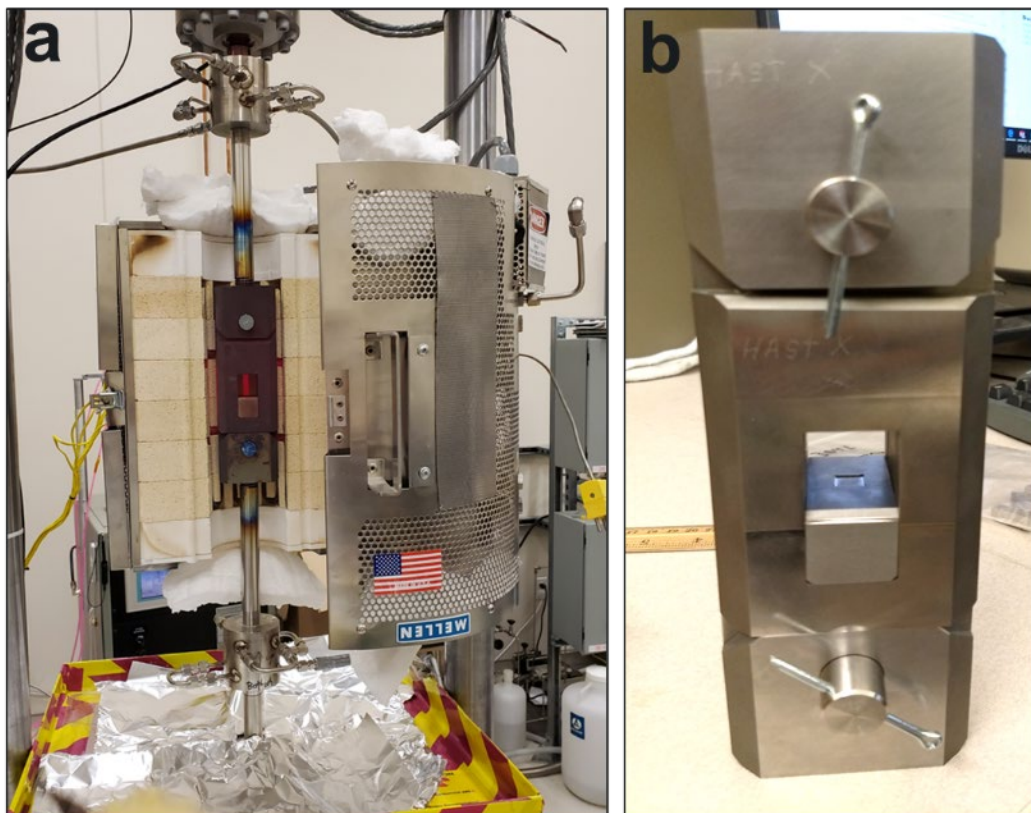
Figure 2-2. Forging equipment: (a) hot forging setup and (b) forging fixture

Table 2.1. Forging sample conditions

Sample Number	Strain Rate (s^{-1})	Initial Thickness (mm) [in]	Final Thickness (mm) [in]	Reduction Percentage
1	0.01	20.4 [0.80]	4.2 [0.17]	79.4
2	0.01	21.0 [0.83]	13.1 [0.52]	37.7
3	0.01	20.3 [0.80]	8.9 [0.35]	56.1
4	0.10	21.2 [0.83]	12.4 [0.49]	41.2
5	0.10	23.4 [0.92]	10.3 [0.41]	55.8
6	0.10	23.4 [0.92]	8.5 [0.33]	63.8

After forging, samples were annealed at 700°C for 120 min. Hot rolling was then performed on each of the six forged-and-annealed samples using a Stanat model TA-215 mill in two-high configuration, with both rolls having a 4" diameter and 8" width. The samples were wrapped in 0.001" thick Zr foil and preheated for 20 minutes at 720°C in a Thermcraft Model 1134 tube furnace, then immediately rolled (within 10 seconds) at 50 rotations per minute. The target for each pass was approximately 20–25% reduction to a final thickness of 0.04". When the sample thickness had reached 0.1", a mid-step anneal at 700°C for 45 minutes was performed. When the hot rolled foils reached 0.04" thick, they were annealed again for 45 minutes at 700°C to fully recrystallize the microstructure before cold rolling.

Cold rolling was performed by adding two 0.875" center rolls to the mill and rolling to 0.0085" at approximately 15–20% reduction per pass. After cold rolling to 0.025", the foils were annealed at 700°C for 45 minutes before the final cold roll to 0.0085". The finished cold-rolled foils were annealed one final time at 700°C for 45 minutes to recrystallize the microstructure. A general flow diagram of the thermomechanical processing can be seen in Figure 2-3. At each stage represented in Figure 2-3, samples were taken for metallography for each of the six forging conditions.
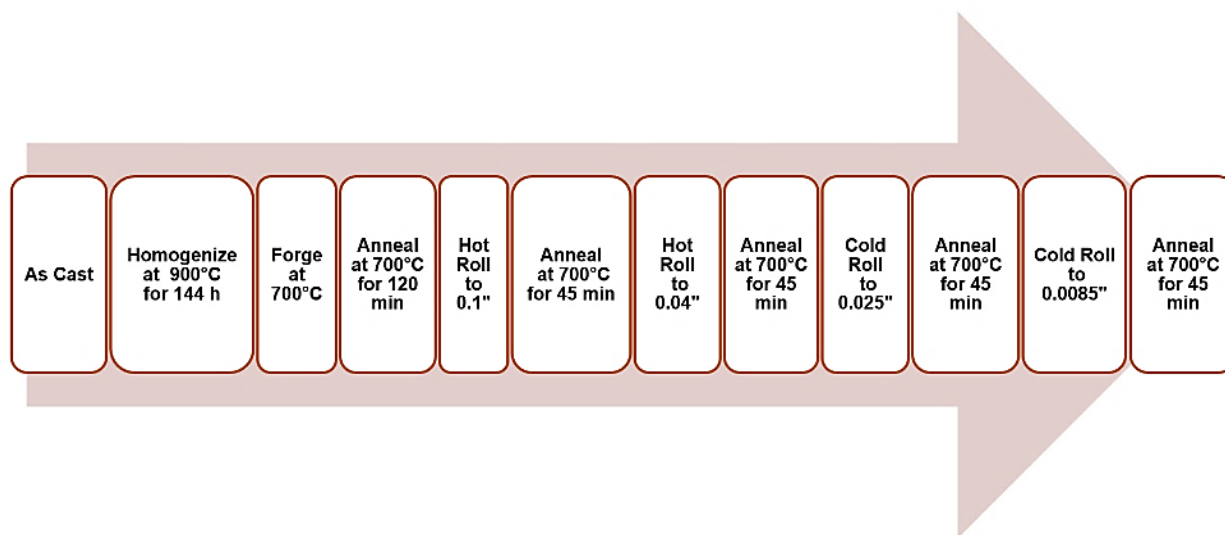
Figure 2-3. Thermomechanical processing summary for this study. Samples were taken for characterization at each of the 12 steps pictured above.

2.3   Bulk Chemistry

Bulk carbon concentration in the cast plate was measured on Thick Casting 5 using a commercial combustion analyzer (LECO C230).

Electropolishing had been performed before carbon concentration analysis to remove any surface oxide. This was conducted using 30% sulfuric acid solution at room temperature and at approximately 3.0 V and 2.0 A for around 2 minutes. The samples were then rinsed with deionized water and allowed to dry in air before being transported to the combustion analyzer.

The combustion analyzer was calibrated using a 1330 ppm carbon single-point linear calibration and was periodically checked during analysis with a certified 664 ppm check standard and blanks to verify the instrument was operating appropriately. Information on the analysis of oxygen, nitrogen, and hydrogen concentrations in the cast plate can be found in (Huber, McCoy, et al. 2021).

Molybdenum analysis was performed by inductively coupled plasma–optical emission spectrometry (ICP-OES).

Before the analysis, electropolishing was performed on 750 mg pieces from the center of the plate. These pieces were dissolved in a concentrated hydrochloric acid and 30% hydrogen peroxide mix. The solution was dried out and diluted in a known volume of 0.5 M nitric acid and

analyzed in triplicate. The results (shown in Table 3.1) are the averages of the triplicate analysis results.

2.4 Sample Preparation and Examination via Optical and Scanning Electron Microscopy

Specimens were sectioned and prepared for optical and scanning electron microscopy (SEM) according to procedures outlined in (Prabhakaran et al. 2016). This includes mounting in epoxy and grinding with silicon carbide paper to a 1200 grit finish, then with 9 μm and 3 μm diamond polishing suspensions. Final polishing was done on a vibratory polisher using 1 μm diamond suspension followed by 0.05 μm colloidal silica suspension.

For metallography via optical microscopy (OM), mounted and polished samples were left in air to oxidize until adequate grain contrast was achieved—typically a minimum of 48 hours. OM was performed using an Olympus BX61M microscope with a three-axis automated stage and digital charge-coupled device camera. OM Images were obtained using bright field mode at magnifications of 2.5×, 10×, 20×, and 50×. A minimum of three images per magnification (left, middle, right) and one 2.5× montage image were taken per specimen using the Olympus Stream Motion software. The montage image provided an overview of the entire specimen through automated image stitching.

For SEM, the polished samples were then coated with ~10 nm gold in an SPI-Module sputter coater to support good conductivity. Microstructural and elemental analyses were carried out using a JEOL JSM-7600F SEM equipped with an Oxford Instruments AZtec X-Max 80 mm^2 energy-dispersive x-ray spectroscopy (EDS) detector and INCA Microanalysis Suite software. Multiple SEM images were taken at 200× or 250×, as well as 1000× magnifications using the Everhart-Thornley detector (lower electron image, LEI) and the low-angle backscattered electron (BSE) detector (LABE or LBE) for each specimen. A few LEI and LABE montage images of the U-10Mo at 250× were also taken to capture a wider field of view. The typical microscope settings used were 30 keV, 15 mm working distance, 110 μm aperture, and beam current of ~6×10^{-9} A or higher. The primary goal of SEM analysis was to analyze uranium carbide (UC) particles and potential chemical banding, inhomogeneity, and defects.

Quantitative chemical analysis was performed using EDS. Spectra were collected at a working distance of approximately 15 mm and a voltage of 30 keV. The EDS was performed using line scans (~350 μm each) at the center of each U-10Mo specimen to evaluate the molybdenum distribution across the specimen thickness at a magnification of 250× and step size of 1 μm. An average of four line scans for each specimen were used to document molybdenum content. During EDS line scanning, x-ray spectra come from the U-10Mo matrix and UC particles. When selecting the line area, UC were carefully avoided so that molybdenum homogeneity could be assessed more accurately. To this end, data values under 7 wt% molybdenum were dismissed as spectral emissions from UC particles.

Electron backscatter diffraction (EBSD) was performed using an FEI Helios NanoLab 660 focused ion beam SEM, EDAX detector, and EDAX/TexSEM Labs (TSL) Orientation Imaging Microscopy (OIM) software. Scans were taken at 30 keV, 13 nA current, and 100× magnification with a 1.1 μm step size. Data cleanup was performed by removing points with low confidence intervals (less than 0.1) followed by one round of confidence interval standardization and grain dilation. All data processing was done using EDAX OIM Analysis v8.

2.5   Data Analysis Methods

Optical micrographs were used to obtain average grain size measurements using a linear-intercept method in accordance with ASTM E112-13, (ASTM International 2021) and ImageJ. To determine the mean grain size of the sample, the line-intercept method was used. Five lines were drawn across the microstructure in each OM image and the lengths of the lines were divided by the number of grain intersections. The software was calibrated using the scale bar in the optical micrograph to attain accuracy. The magnification used to obtain these measurements varied with processing condition and grain size. As-forged and as-rolled samples were too heavily deformed to achieve accurate grain size results using this method. Therefore, only heat-treated microstructures such as homogenized, forged and annealed, and hot or cold rolled and annealed were measured using the line-intercept method. Grain size data from EBSD were obtained on two of the forged-and-annealed conditions (as-forged Samples 1 and 2) and were compared to the data obtained through OM on these samples.

The UC area (μm^2) and area fractions were analyzed using BSE SEM images and ImageJ analysis software. Manual thresholding was used to distinguish UC particles (dark area) from the matrix. The particle size range was 0-infinity μm^2 and the circularity rage limitation was 0-1 with 1 being a perfect circle[1]. The area of the UC particle was (calculated as the sum of the areas of each pixel (converted to μm) within the borders of the particle. An example of this thresholding can be seen in Figure 2-4. Image magnifications of 200×, 1000×, or both were used in the analysis depending on the UC size and volume fraction of the sample. Between 400 and 2000 UC particles were examined per sample condition.
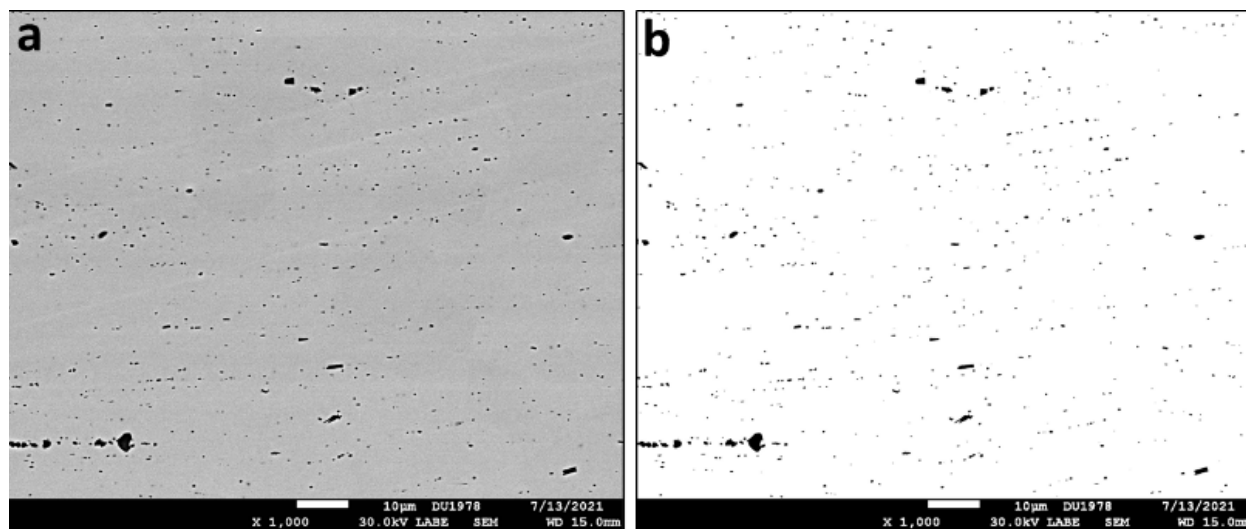
Figure 2-4. Example of thresholding using ImageJ to determine UC size and area fraction: (a) BSE image of as-forged Sample 2 after final cold rolling and annealing and (b) the same BSE image after thresholding using ImageJ

Statistical analysis software Minitab was used to compare the mean grain and UC size data obtained from image analysis. A Welch's analysis of variance (ANOVA) with a post-hoc Games-Howell test was used to assess the differences among the means for each of the six samples.

---

[1] $4\pi \times \dfrac{Area}{Perimeter^2}$

This test was the most appropriate because data analyzed in this study due have non-normal distributions and potential for unequal variances.

3.0   Results and Discussion

The results obtained from the materials and methods outlined above are presented and discussed in this section. This includes data from chemistry, SEM, and OM techniques. Some OM images and other data not displayed in this section can be found in the Appendix.

3.1   Thick Plate 5 As-Cast and Homogenized Conditions

3.1.1   Bulk Chemistry

The average molybdenum and bulk carbon content of Thick Plate 5 are displayed in Table 3.1. Data were collected at three plate locations (top, middle, and bottom). The average bulk carbon content of the plate was 189 ± 21 ppm, where ± 21 refers to plus or minus the standard deviation of the data—the typical dispersion of the data about the mean. The average molybdenum concentration was 11.0 ± 1 wt%. Thus, the average bulk carbon content for this plate was low—substantially lower than the U-10Mo fuel specifications of ≤ 800 ppm and the requirements for other U-10Mo studies[1] (INL 2018; Huber, McCoy, et al. 2021; Kalsar et al. 2020). The molybdenum content was slightly higher than the 10.0 ± 1 wt% specification but is not a concern for the scope of this study. Knowledge of the plate carbon content and molybdenum concentration is important for making sure the plate meets the qualification standards. It is also vital for understanding microstructure development during the subsequent thermomechanical processing.

Table 3.1. Bulk chemistry results. The spread of the data is represented as plus or minus (±) the standard deviation.

Sample Location	C (ppm)	Mo (wt%)
Top	219	11.8
Middle	178	9.6
Bottom	171	11.7
Average	189 ± 26	11 ± 1

3.1.2   Chemical Analysis via EDS

The as-cast U-10Mo microstructure is an inhomogeneous and dendritic, with molybdenum-rich (brighter) regions and molybdenum-lean (darker) regions, as can be seen in Figure 3-1. The goal of homogenization is to create more consistent microstructure and uniform distribution of molybdenum throughout the plate. Proper molybdenum distribution is important because molybdenum segregation can cause body-centered cubic (BCC) γ-phase instability and create the undesirable orthorhombic α-phase during subsequent thermal processing. The homogenization of Thick Plate 5 was performed above the γ-phase field temperature (560°C) at 900°C for 144 h, which was previously identified as an acceptable condition for U-10Mo homogenization (Joshi, Nyberg, Lavender, Paxton, and Burkes 2015; S. Jana et al. 2019).

To evaluate the molybdenum distribution, quantitative chemical analysis (EDS) was performed on Thick Plate 5 in the as-cast and the homogenized conditions. Care was taken to try to avoid

---

[1] NL. 2018. Specification for Low Enriched Uranium Monolithic Fuel Plates. SPC-1635, Rev. 10. Idaho Falls, ID: Idaho National Laboratory

carbides during the line scans to gain a more accurate representation of molybdenum segregation. Four line scans approximately 350 μm long were taken at different locations of the plate at a 250× SEM magnification. Representative line scan data for the as-cast and the homogenized conditions are displayed in Figure 3-1 and Figure 3-2. In the as-cast condition, the molybdenum concentration varies considerably across the sample area (7.0–11.9 wt% molybdenum), with an average of 9.4 ± 1.1 wt% molybdenum among the four line scans. Upon homogenization at 900°C for 144 h, the molybdenum concentration becomes more uniform across the microstructure, as displayed in Figure 3-1b and Figure 3-2b. The molybdenum content ranged between 7.9 wt% and 10.3 wt%, with an average of 9.6 ± 0.2 wt% molybdenum among the four scans performed. Points with less than 7 wt% molybdenum were locations where the spectra encountered carbides and were not included in the molybdenum content analysis. Often these data points visibly crossed over large carbides in the SEM line scan image. Six points were removed for the as-cast dataset and one for the homogenized dataset. The EDS results confirm sufficiently uniform distribution of molybdenum after homogenization and are reasonably close to the 10.0 ± 1 wt% molybdenum specification. Variation between molybdenum concentrations obtained from EDS and those obtained from ICP-OES can be attributed to the limitations of EDS for quantitative analysis.
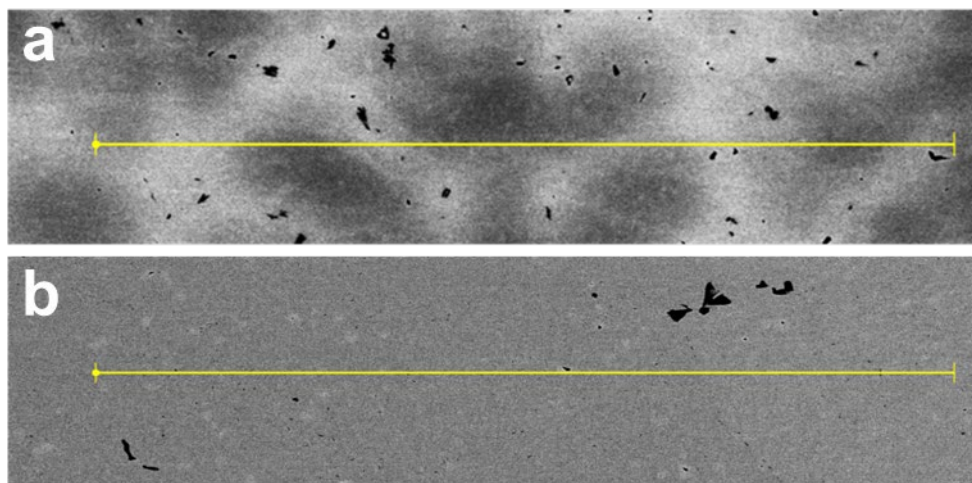

Figure 3-1. EDS line scan locations on Thick Casting 5: (a) as cast and (b) homogenized
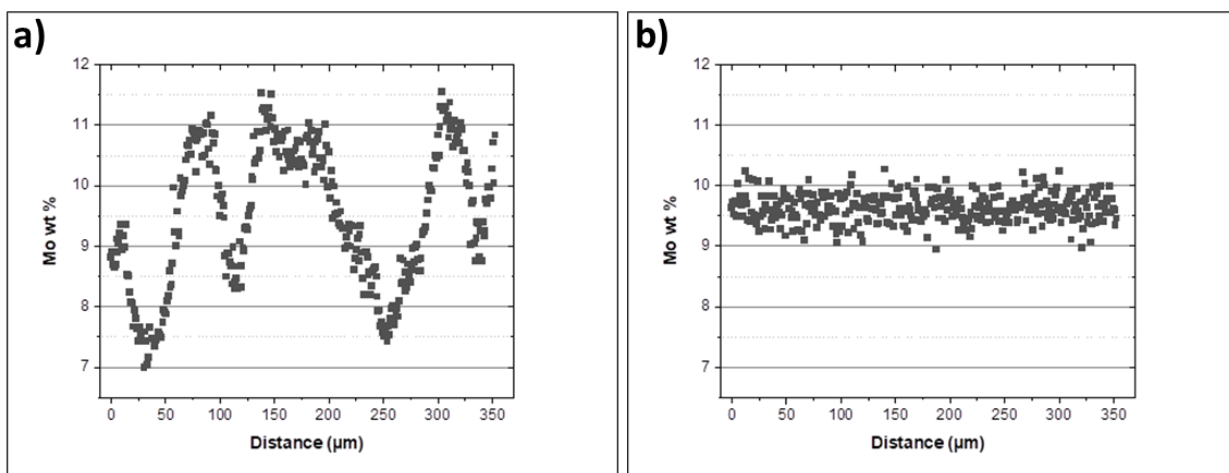
Figure 3-2. The molybdenum weight percentage variation across the EDS line scan areas displayed in Figure 3-1 for (a) Thick Plate 5 as cast and (b) Thick Plate 5 after homogenization

3.1.3   Morphology

The microstructure of Thick Plate 5 was analyzed via OM and SEM before and after homogenization. Overview montages at 2.5× and 10× of optical micrographs of both conditions can be seen in Figure 3-3 and Figure 3-4, respectively. The Thick Plate 5 as-cast microstructure is dendritic and matches the morphology commonly seen in as-cast U-10Mo (Huber, McCoy, et al. 2021; Kalsar et al. 2020; Joshi, Nyberg, Lavender, Paxton, and Burkes 2015; S. Jana et al. 2019; Xu et al. 2016). The microstructure consists of molybdenum-rich dendrites (lighter contrast) and molybdenum-lean interdendritic regions (darker contrast), showing that the molybdenum-lean regions solidified under nonequilibrium conditions. The average primary dendrite arm length was 380 ± 9 µm and is comparable to those in other U-10Mo castings with similar carbon contents (Huber, McCoy, et al. 2021). Upon homogenization, the heterogeneous, dendritic structure was transformed into an equiaxed, coarse-grained microstructure with limited molybdenum segregation (Figure 3-3 and Figure 3-4). Grain size data is summarized in Table 3.2. The average grain size of the homogenized plate was 833 ± 149 µm and obtained by OM. This large grain size in the homogenized plate reflects a low carbon content, as observed in chemistry and ImageJ analysis. It is widely understood that second phase particles such as UC can cause grain pinning and in general, a higher volume of second phase particles results in finer grained materials (William E. Frazier et al. 2018; Humphreys and Hatherly 2004).
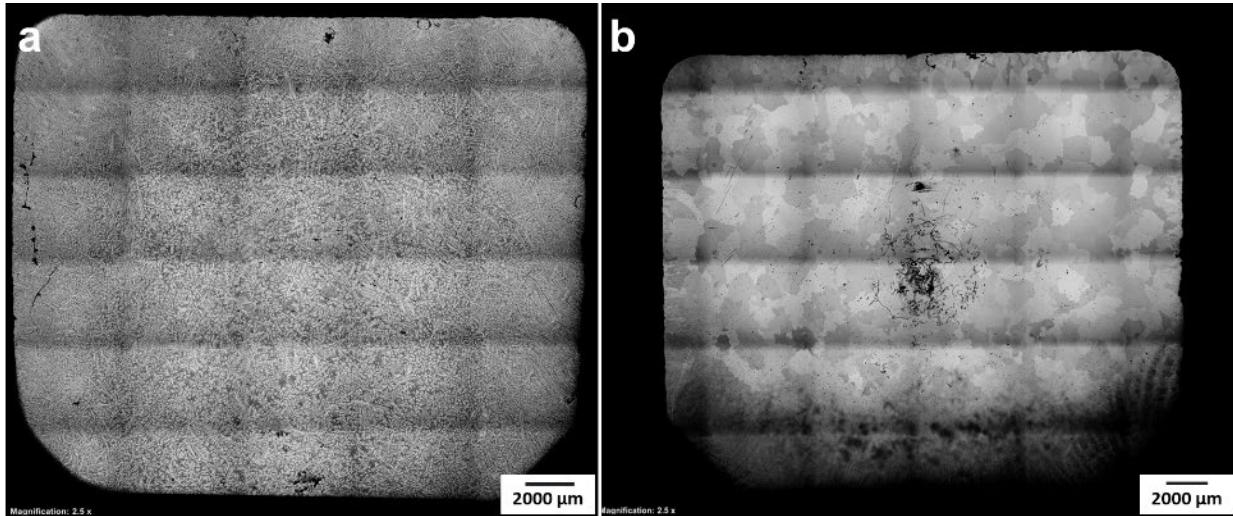
Figure 3-3.   Optical microscopy montage images at 2.5× magnification of Thick Plate 5: (a) as cast and (b) homogenized
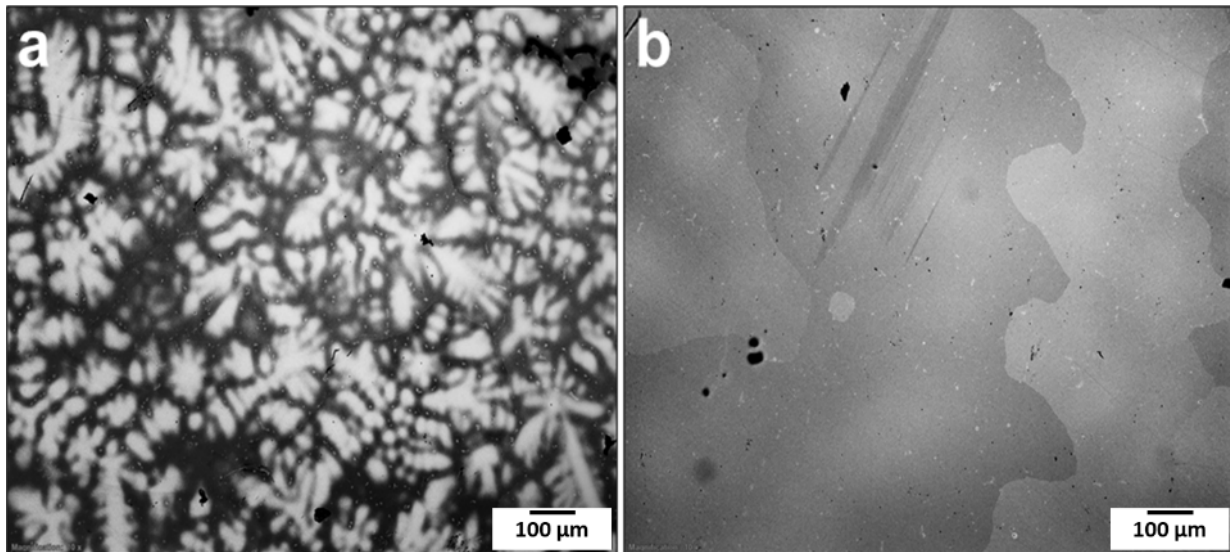
Figure 3-4. Optical micrographs of Thick Plate 5: (a) as cast and (b) homogenized, taken at 10× magnification

The average carbide size (cross-sectional area) in the as-cast plate was 2.9 ± 4 μm², with an average area fraction of 0.51%. This information can be found in Table 3.2 and representative BSE images of the as-cast and the homogenized conditions in Figure 3-5. This carbide size is within the range reported in other U-10Mo studies, and the area fraction of 0.51% is representative of a low carbon content (William E. Frazier et al. 2018; Hu et al. 2018; Kalsar et al. 2020). The average carbide size after homogenization was 2.0 ± 12 μm² with an area fraction of 0.31%. The mean carbide size for the homogenized plate had a much larger spread and a Games-Howell pairwise comparison deemed it not significantly different from the mean size for the as-cast plate. Carbide content analysis on BSE images at either 250× or 1000× magnification indicated totals of 446 UC particles for the as-cast condition and 757 UC particles for the homogenized condition.

Table 3.2. Thick Plate 5 UC and grain size data for the as-cast and homogenized conditions. NA indicates features that are insignificant in a given processing condition and were not measured.

Processing Description	Average UC Size (μm^2)	UC Area Percentage (%)	Average Dendrite Arm Length (μm)	Average Grain Diameter (μm)
As Cast	2.9 ± 4	0.51	380 ± 9	NA
Homogenized	2.0 ± 12	0.31	NA	833 ± 149
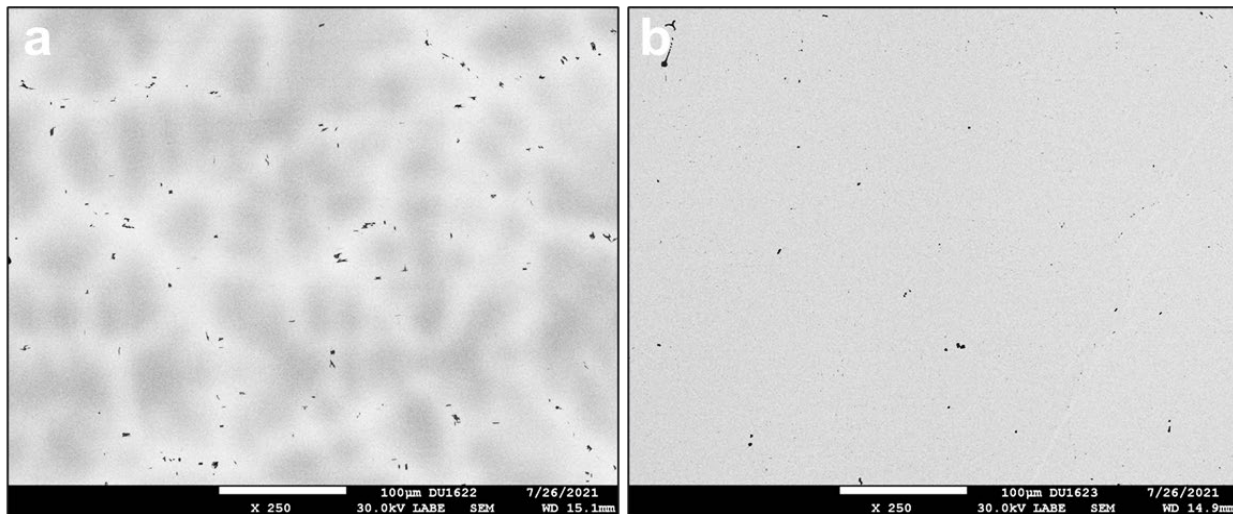
Figure 3-5. BSE images emphasizing UC particles (small black features) of Thick Plate 5: (a) as cast and (b) homogenized, at 250× magnification

3.2   Forged Morphology

3.2.1   Microstructure and Optical Microscopy

Optical micrographs of the as-forged samples for each of the six conditions can be seen in Figure 3-6 and Figure 3-7. All six forging conditions resulted in similar morphology, consisting of courser grains surrounded by very fine recrystallized grains. The presence of these fine recrystallized grains surrounding larger deformed grains in the as-hot forged state was confirmed using high magnification EBSD (Figure 3-10) and will be discussed later. OM of the as-forged and forged annealed states indicate dynamic recrystallization occurred during the hot forging process followed by further growth during the 700°C 2h anneal. Maintenance
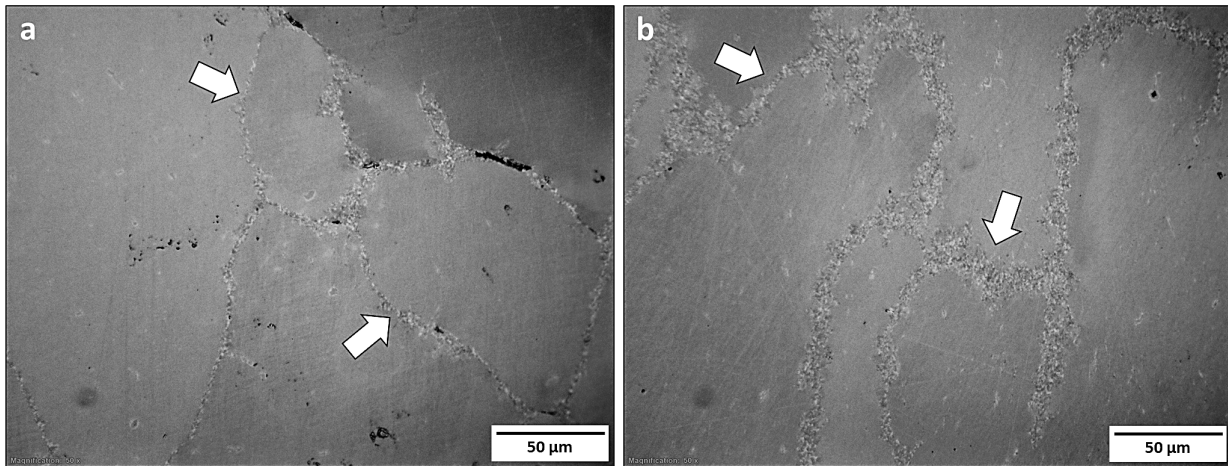
Figure 3-6. Representative optical micrographs taken at 50× of (a) as-forged Sample 2 and (b) as-forged Sample 3, showing fine grain formation along the boundaries of coarse grains.
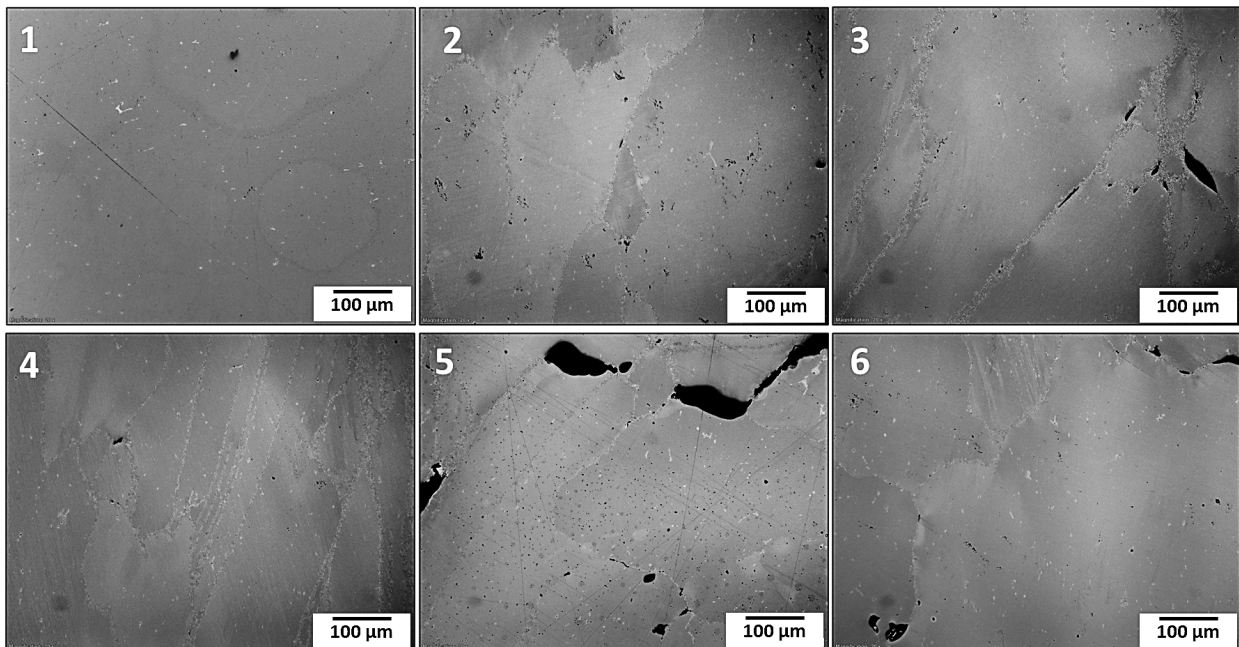
Figure 3-7. OM images taken at 20× for the six different forging conditions before annealing. Samples 1–6 are labeled accordingly. Micrographs display strained, as-forged microstructure, particularly along grain boundaries.

The grain boundaries of larger coarse grains served as energetically favorable sites for nucleation and growth of new grains during deformation and annealing (Humphreys and Hatherly 2004). Evidence of this can be seen in Figure 3-8, which displays micrographs taken of the as-forged samples after annealing at 700°C for 2 h. Here, smaller, strain-free grains populate the grain boundaries of larger, deformed grains, forming a "necklace" structure. The classification of these grains as "deformed" or "strain-free" is justified in the following section on EBSD. Overall, the results of the forging and annealing procedures was a heterogeneous

microstructure and large variation in grain size. This heterogeneity in the microstructure is quantitatively represented in Figure 3-9, where the average grain size for each condition and its standard deviation are plotted. Table 3.3 summarizes the average grain size and lists statistics groupings for each of the six forging conditions. Depending on the sample conditions, the average grain size obtained from OM ranged from 23–371 µm. This is significantly smaller than the mean grain size of 833 µm for homogenized samples, as is evident in Figure 3-9a. Thus, the forging procedure reduced the average grain size. A graph comparing the grain size of the homogenized condition to all subsequent hot working operations is shown in Figure A.2 in the appendix.
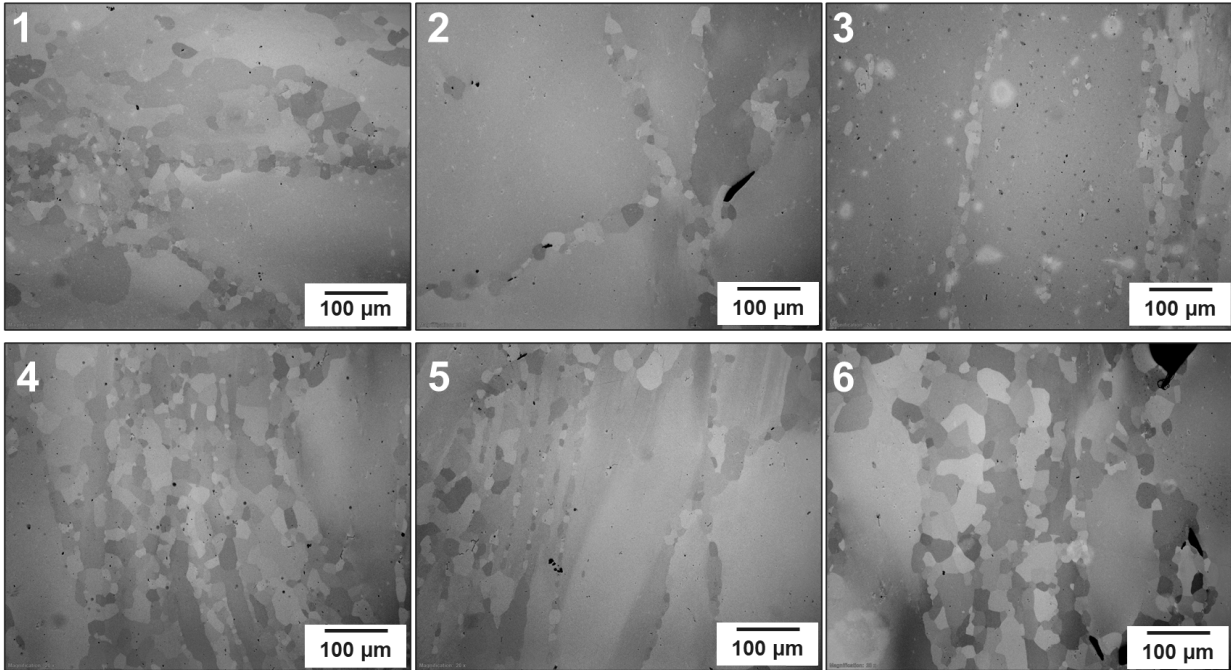

Figure 3-8. OM images taken at 20× for the six different forging conditions after forging and annealing for two hours at 700°C. As-forged Samples 1–6 are labeled accordingly.
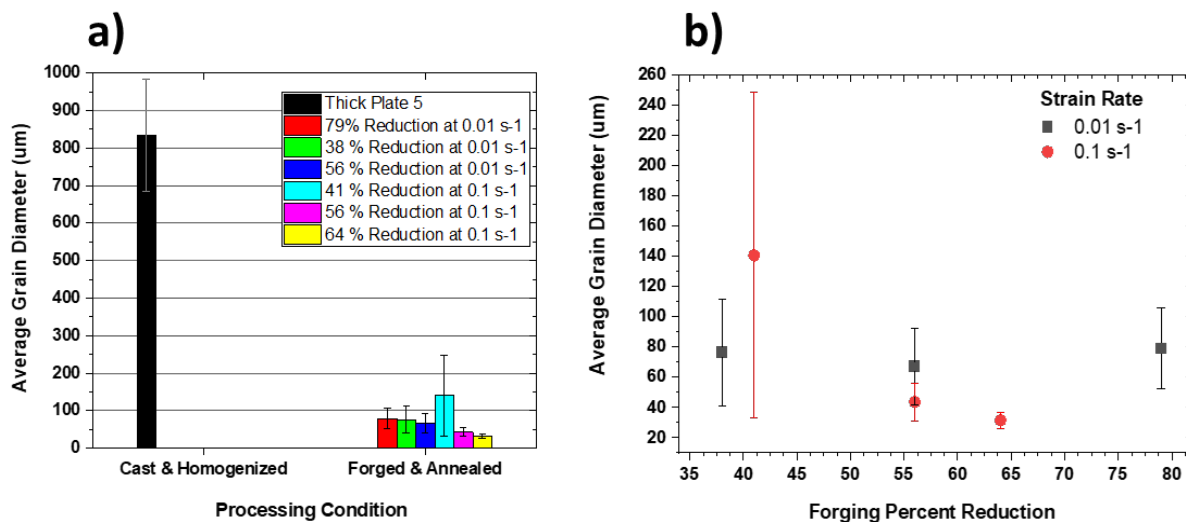
Figure 3-9. Grain size data from OM: (a) bar graph comparison of the average grain diameters from OM after homogenization and forging plus annealing for all six samples; (b) plot comparing the average grain diameter from OM (after forging and annealing) to the reduction percentage during forging for each of the two strain rates

Table 3.3. Grain size information after hot forging and annealing. Mean values that do not share a letter are significantly different.

Forged Sample Number	Reduction Percentage	Forging Strain Rate (s^{-1})	Mean Grain Size from OM (μm)	Statistical Grouping from OM	Mean Grain Size from EBSD (μm)	Statistical Grouping from EBSD
1	79.4%	0.01	79 ± 27.8	A	16.3 ± 22.9	A
2	37.7%	0.01	76 ± 36.3	A	17.5 ± 42.4	A
3	56.1%	0.01	67 ± 26.3	AB	*	*
4	41.2%	0.10	141 ± 111.5	A	*	*
5	55.8%	0.10	44 ± 13.0	B	*	*
6	63.8%	0.10	32 ± 5.47	C	*	*

* Data was not collected on this sample condition

Despite variation in the grain size across the six samples, no significant correlation between the reduction percentage or strain rate and the final forged and annealed grain size was concluded using OM. A one-way ANOVA Games-Howell pairwise comparison of the means using grain size data obtained from OM indicated a significant difference in the mean grain size at 64% reduction (Forged 6) and all five other reduction percentages. There was also a statistically significant difference between as-forged Sample 5 (55.8%, 0.1 s^{-1}) and Samples 1 (79.4% 0.01 s^{-1}), 2 (37.7% 0.01 s^{-1}), 4 (41.2%, 0.1 s^{-1}), and 6 (63.8%, 0.1 s^{-1}). As-forged Samples 1–4 had no statistically significant difference among their mean grain sizes. The mean grain size for samples with different strain rates but similar reduction percentages, such as those of as-forged Samples 3 and 5, had no statistically significant difference between their mean grain sizes.

These statistics are summarized in Table 3.3, where letter groupings identify whether the means are significantly different or not (only means that do not share a letter are significantly different).

When examining the data obtained from OM, it is important to consider the small sample size and the limitations of using the line-intercept method for grain size estimations of heterogeneous microstructures (ASTM E112-13). More data are needed to accurately compare and derive conclusions on the effect of forging conditions on the grain size after final forging and annealing. Though the Games-Howell comparison resulted in a statistically significant difference among the grain sizes for a few of the conditions, it is important to note that this was a limited sample size (200–600 grains examined per sample). Also consider that the grain size and morphology varied significantly with the location of the OM image. This likely created a sampling bias and makes it difficult to capture the entire microstructure in just three OM images. To indicate the extent of morphology variation across each sample, montage images are provided in Figure A.3 in the appendix. More data and EBSD analysis are needed to illustrate the effects of strain rate and forging reduction on the resulting microstructure and recrystallization kinetics. A limited EBSD analysis on as-forged and as-forged annealed Samples 1 and 2 is discussed in the next section.

3.2.2   Electron Backscatter Diffraction

EBSD was performed on Sample 2 (37.7% reduction at 0.01 s−1) in the as-forged condition and after forging and annealing on Sample 1 (79.4% reduction at 0.01 s−1) and Sample 2. The results from EBSD on the as-forged Sample 2 support observations from OM regarding the occurrence of dynamic recrystallization during hot forging. Figure 3-10 displays orientation maps along with grain orientation spread (GOS) maps taken at two different magnifications of the as-forged Sample 2. Orientation and GOS maps of Samples 1 and 2 after forging and annealing can be seen in Figure 3-11. In both figures, the GOS maps highlight grains with more than 2° GOS in blue and those with less than 2° GOS in red to differentiate nucleated, strain-free grains from the larger, deformed grains. GOS is a common grain-based method for evaluating plastic strain using local misorientations. During deformation, dislocations accumulate in a material which cause variations in the crystal lattice (misorientations) which can be detected using EBSD. The GOS represents the orientation deviations of the pixels within a grain relative to the average orientation of that grain. This criteria of GOS < 1–3° denotating recrystallized grains has been used previously. (Reeve et al. 2022; Wright, Nowell, and Field 2011; Adam, Long, and Field 2017; Dziaszyk et al. 2010; Humphreys and Hatherly 2004). The average percent of recrystallized grains after forging to 37.7% reduction at 0.01 s−1 (Sample 2) was 3% in the 250x magnification EBSD scan. Due to the fine grain size, the average grain diameter value for the recrystallized grains (GOS < 2°) was collected from the 5000x magnification scan and was 2.85 ± 1.90 µm. A total of 21 grains were analyzed. EBSD was only performed on Sample 2 in the as-forged case, however, based on OM similar microstructures occurred in the other forging conditions.
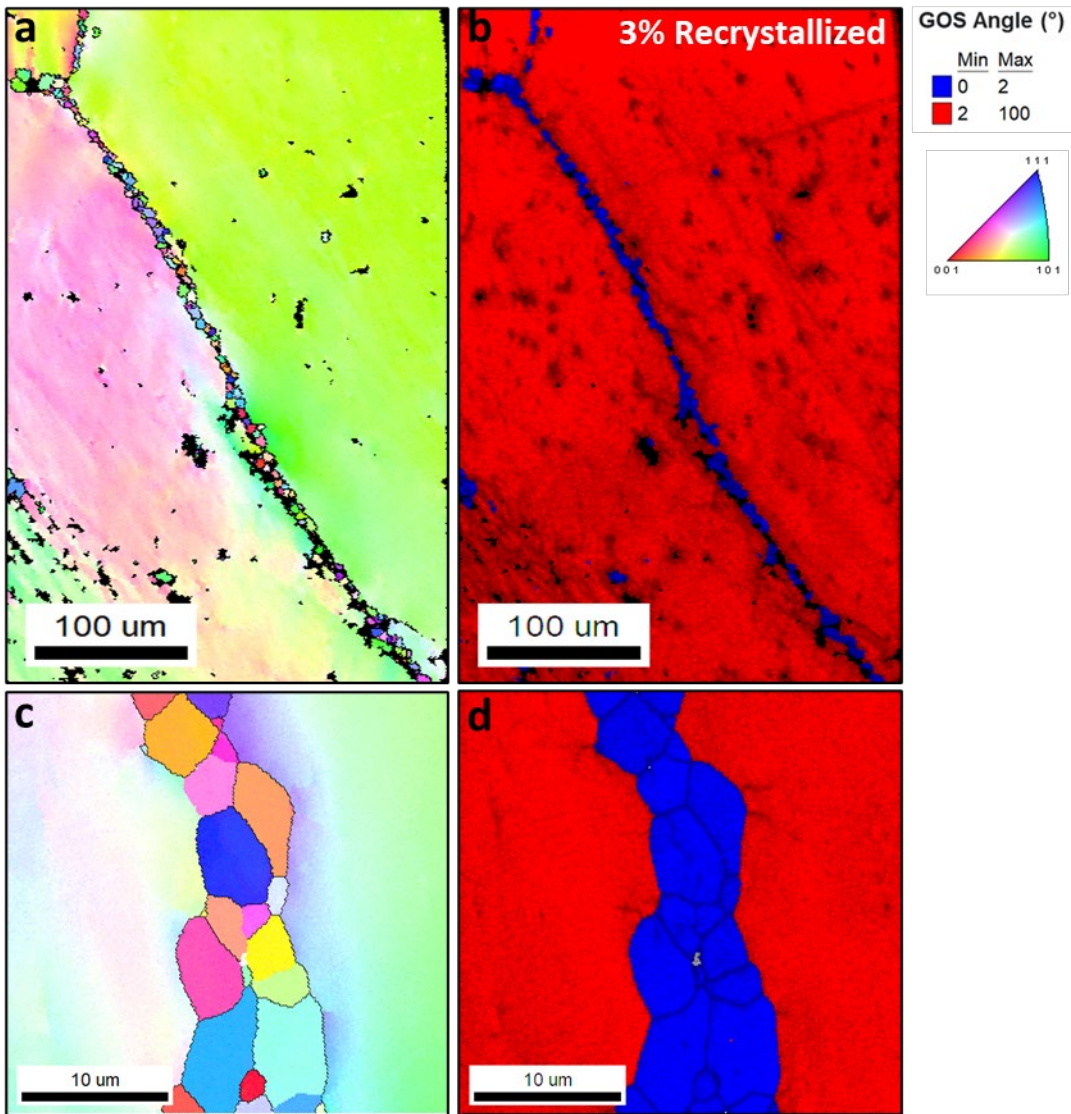
Figure 3-10. Orientation and GOS maps of forged sample 2 after hot forging prior to annealing. Scans taken at 250x (a,b) and 5000x (c,d). GOS maps depict small, recrystallized grains (blue) surrounding larger deformed grains (red).
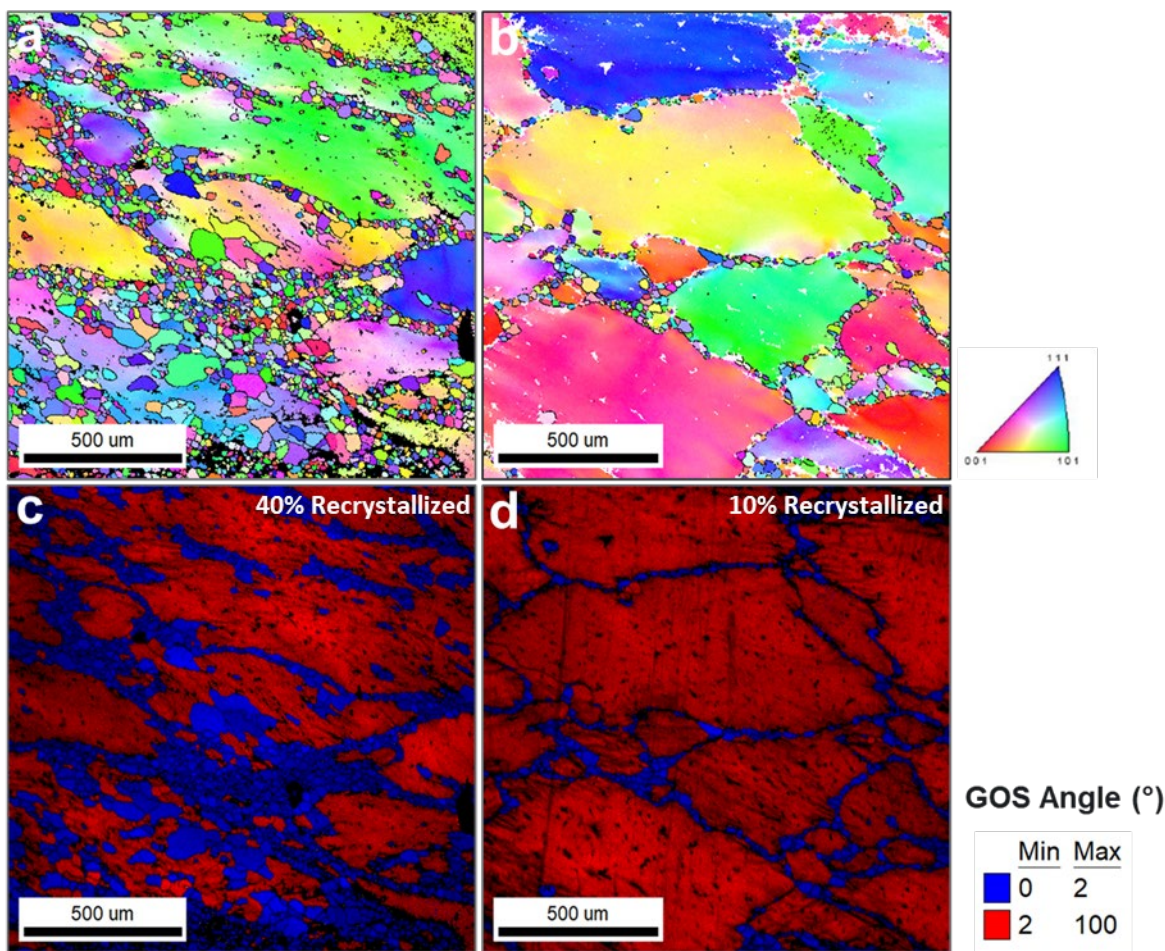
Figure 3-11. Orientation and GOS maps after forging and annealing of Sample 1 (a, c) and Sample 2 (b, d) taken at 100× magnification. GOS maps depict small, recrystallized grains (blue) surrounding larger deformed grains (red).

The average grain sizes obtained from EBSD of as-forged and annealed Samples 1 and 2 were 16.3 ± 22.9 µm and 17.5 ± 42.4 µm, respectively. EBSD was not able to capture the entire area of the larger deformed grains at the 100× magnification, resulting in larger grains being underrepresented in these data despite edge grains being included in the size analysis. The average grain sizes from EBSD differ significantly from those obtained using OM (Table 3.3). This difference was attributed primarily to the fact that substantially more grains were analyzed using EBSD than OM: EBSD analysis included 3089 analyzed from as-forged Sample 1 and 1172 from as-forged Sample 2; OM analysis included only 256 and 224 grains from Samples 1 and 2, respectively. Based on the Games-Howell pairwise comparisons, no significant statistical difference is apparent between the mean grain sizes (obtained by EBSD) of as-forged Samples 1 and 2. The statistical grouping for these means is included in Table 3.3. Thus, the reduction percentage apparently has no appreciable effect on the final grain size after forging and annealing. However, more EBSD scans at different locations are needed to state this conclusively.

The reduction percentage does appear to have a significant effect on the kinetics of recrystallization, as expected. As-forged annealed Sample 2 (38% reduction) appears to have

fewer recrystallized grains than as-forged Sample 1 (79% reduction). The GOS results confirm this: Forged Sample 2 had 10% recrystallized grains and GOS < 2°, whereas as-forged Sample 1 had 40% and GOS > 2°. This implies that increasing the forging reduction percentage quickened the recrystallization kinetics and resulted in the nucleation of more strain-free grains under the same annealing parameters. This result is to be expected; it is widely known that an increase in reduction percentage or deformation typically increases the rate of recrystallization during annealing (Humphreys and Hatherly 2004). For as-forged Sample 1, the average diameter of grains with GOS < 2° (recrystallized) was 14.9 ± 10.8 µm, whereas for those with GOS > 2° (deformed) it was 81.2 ± 118.4 µm. A total of 3020 recrystallized and 69 deformed grains were analyzed. As-forged Sample 2 had an average GOS < 2° grain size of 12.4 ± 8.5 and a GOS > 2° grain size of 158.0 ± 171.9 µm. A total of 1131 recrystallized grains and 41 deformed grains were analyzed for as-forged Sample 2. The orientation maps did not indicate any preferred orientation or texture of U-10Mo after forging and annealing. A random texture has also been observed in rolled and annealed U-10Mo samples (Schuessler et al. 2021; Reeve et al. 2022).

Understanding the effects of hot forging conditions on the recrystallization kinetics is important for optimizing annealing time and temperature so that the desired microstructure prior to rolling is achieved. As discussed previously, the starting microstructure influences the subsequent processing and the potential for defects. More EBSD analysis and annealing studies would need to be performed to quantify the recrystallization kinetics of U-10Mo hot forging and the effects of different forging conditions.

3.2.3   Molybdenum Homogeneity (EDS)

EDS was performed on as-forged Sample 1 (79.4% Mo, 0.01 s^{-1} strain rate) on four different locations at 250× magnification. Representative line scan data is shown in Figure 3-12. EDS results showed molybdenum content between 8 and 11 wt%, with an average of 9.6 ± 0.4 wt% molybdenum. These values are comparable with those from the homogenized state prior to forging (9.6 ± 0.2 wt% molybdenum), and therefore confirm that forging had no obvious effect on molybdenum homogeneity.
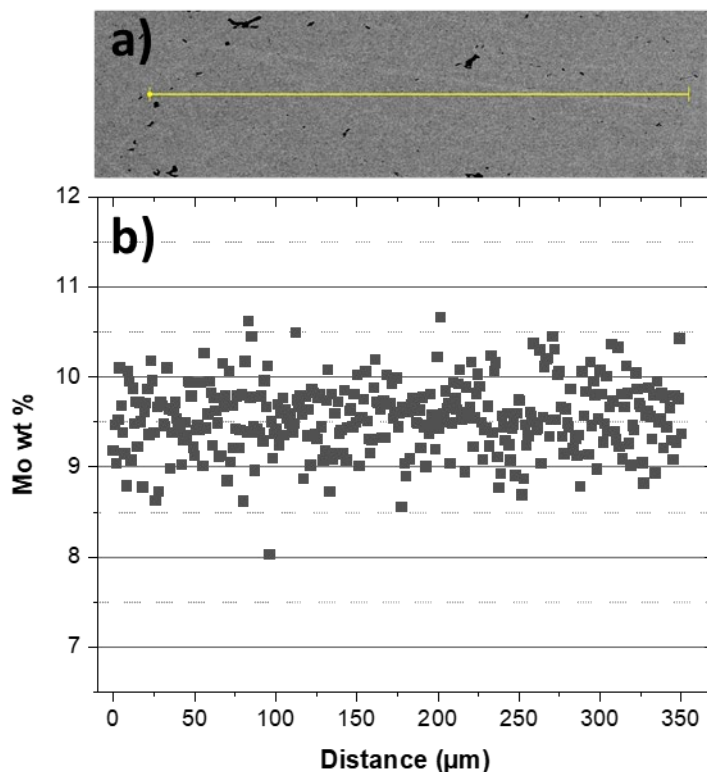
Figure 3-12. EDS information: (a) line scan location and (b) molybdenum content variation

3.2.4   Carbides and BSE Analysis

BSE images showing carbide morphologies for the various forging conditions before and after annealing are displayed in Figure 3-13 and Figure 3-14. 1000 – 2000 carbides per sample in the annealed condition, and 500 – 750 carbides per sample in the as-forged condition were analyzed via ImageJ for particle area and area fraction. This analysis indicated no statistically significant difference in mean UC particle size for any of the forging conditions before annealing.

The UC particle size across the six forging conditions ranged from 0.002 to 109 μm^2, with an average of 0.35 ± 3.0 μm^2, before annealing. Carbide size and area percentage values for all six forging conditions are summarized in Table 3.4 and Table 3.5. The average area fraction of UC particles was 0.54 for the as-forged condition and 0.56 for the forged-and-annealed samples. Figure 3-15 displays plots of the average UC particle size and interval spread for the as-forged and forged, annealed conditions. After annealing, the average UC particle size over all six conditions was 0.74 ± 2.5 μm^2, though it appeared to vary with reduction percentage, as demonstrated in Figure 3-15. This variation is more likely attributable to SEM image location and limited sample number than to forging condition. As discussed previously, the microstructure is very heterogeneous and varies significantly across the sample. The average UC particle size also appeared to increase after annealing. While it is possible that there is a slight coarsening after annealing, it is not likely that the UC particles grew by the extent recorded here, particularly because the average UC particle size remained fairly consistent throughout subsequent rolling procedures. Thus, the increase in average UC particle size was attributed to the low magnification (200×) images used. Because of this low magnification,

smaller carbides were likely missed during the analysis. The limited sample size and heterogeneous microstructure also factor into this discrepancy.
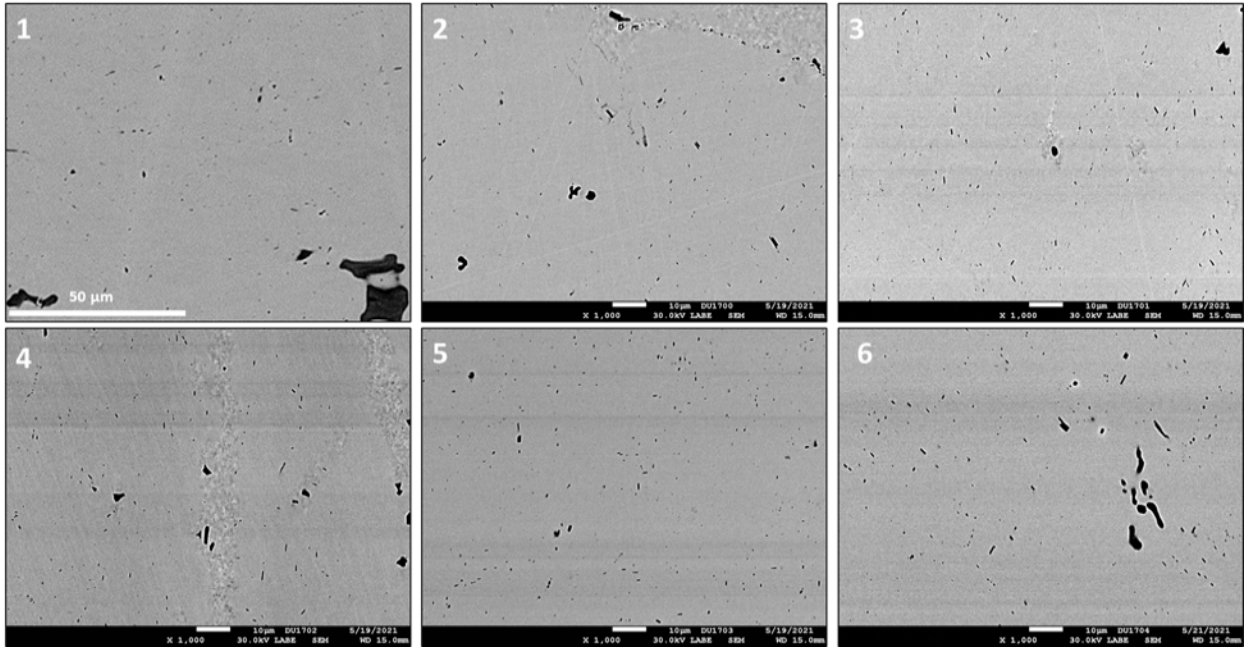

Figure 3-13. BSE images of the six samples in the as-forged conditions taken at 1000× magnification, labeled accordingly
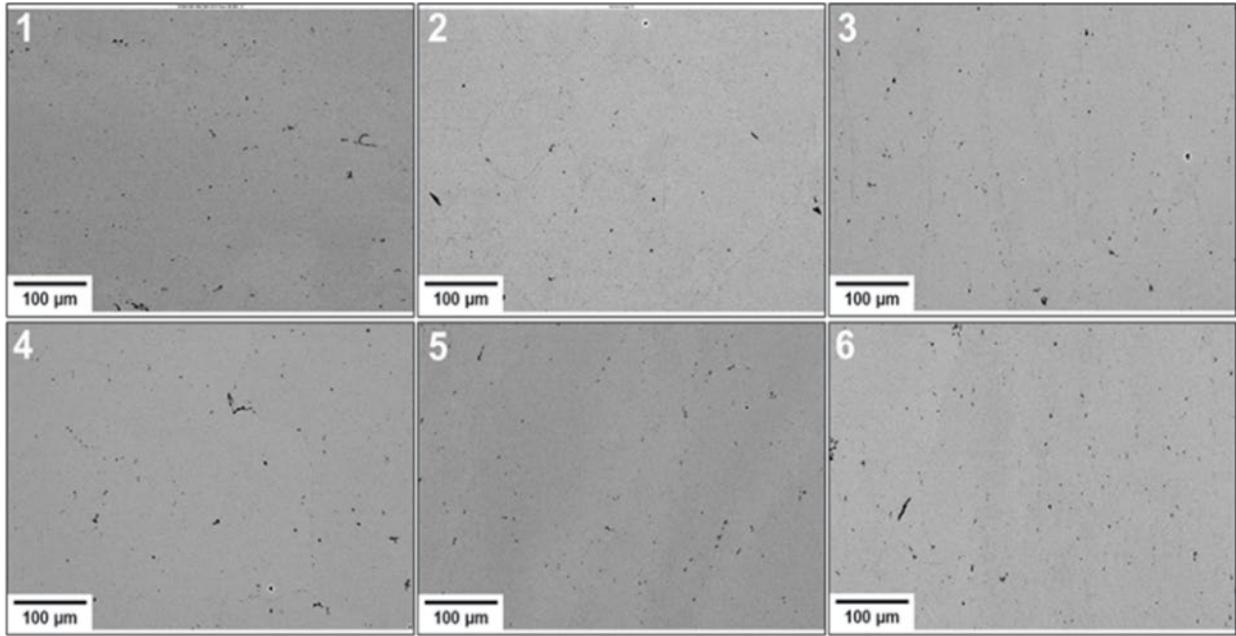

Figure 3-14. BSE images taken at 200× after forging and annealing for all six forging conditions, labeled accordingly

Table 3.4. Average UC Particle Size for the as-forged and the forged-and-annealed conditions. Between 500 and 750 UC particles were analyzed per sample (1–6) in the as-forged condition and 1000–2000 UC particles per sample in the annealed condition.

As-Forged Sample Number	Reduction Percentage	Particle Size (μm^2)	
		As Forged	Forged and Annealed
1	79.4%	0.74 ± 5.81	1.13 ± 3.21
2	37.7%	0.20 ± 0.71	1.22 ± 3.80
3	56.1%	0.19 ± 1.11	1.66 ± 3.26
4	41.2%	0.17 ± 0.81	2.33 ± 5.71
5	55.8%	0.26 ± 1.17	1.42 ± 3.50
6	63.8%	0.53 ± 3.73	1.55 ± 3.81
	Average	0.35 ± 3.00	1.53 ± 3.95

Table 3.5. Carbide area percentage for the as-forged and the forged-and-annealed conditions. Between 500 and 750 UC particles were analyzed per sample (1–6) in the as-forged condition and 1000–2000 per sample in the annealed condition.

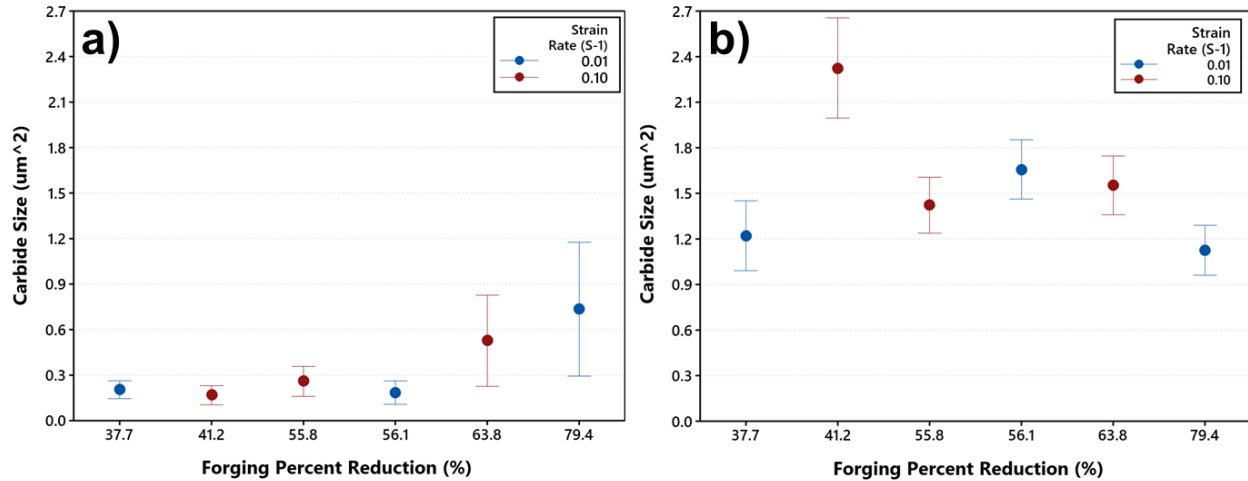| Sample Number	Reduction Percentage	Area Percentage	
		As Forged	Forged and Annealed
1	79.4%	1.14 ± 0.86	0.41 ± 0.10
2	37.7%	0.36 ± 0.04	0.32 ± 0.02
3	56.1%	0.42 ± 0.12	0.29 ± 0.04
4	41.2%	0.33 ± 0.15	0.43 ± 0.06
5	55.8%	0.44 ± 0.23	0.33 ± 0.07
6	63.8%	0.75 ± 0.50	0.38 ± 0.01
	Average	0.61 ± 0.51	0.35 ± 0.07

Figure 3-15. Plots of the average carbide size (a) after forging and (b) after forging and annealing, for all six forging conditions. Error bars represent the interval spread of the data at a 95% confidence interval. Horizontal access distributed evenly among six samples (values) and not to scale.

3.3 Rolling Morphology

3.3.1 Microstructure and Optical Microscopy

Optical micrographs of all six samples after rolling to 0.4" plus annealing and after cold rolling to 0.0085" plus annealing are shown in Figure 3-16 and Figure 3-17, respectively. OM of the hot and cold rolling steps not shown here are displayed in the appendix as Figure A.4 through Figure A.9. This includes the following conditions: as rolled to 0.1" (Figure A.4), hot rolled to 0.1" and annealed (Figure A.5), as hot rolled to 0.04" (Figure A.6), as cold rolled to 0.025" (Figure A.7), cold rolled to 0.025" and annealed (Figure A.8), and as cold rolled to 0.00085" (Figure A.9). The microstructure after final hot rolling to 0.04" and annealing for 45 minutes at 700°C was consistent across all six forging conditions (Figure 3-16). As shown in Figure 3-16, the samples were fully recrystallized and homogeneous, with an average grain diameter of 17 ± 2 μm. The average grain size and standard deviation for each forging condition after hot rolling and annealing are displayed in Table 3.6 and Figure 3-18, respectively. A Games-Howell Pairwise comparison of the means confirmed there was no statistically significant difference in mean grain size after hot rolling and annealing for the various forging conditions. Therefore, neither the starting forged-and-annealed microstructure nor the original forging reduction percentage affected the grain size after hot rolling to 0.04" and annealing.
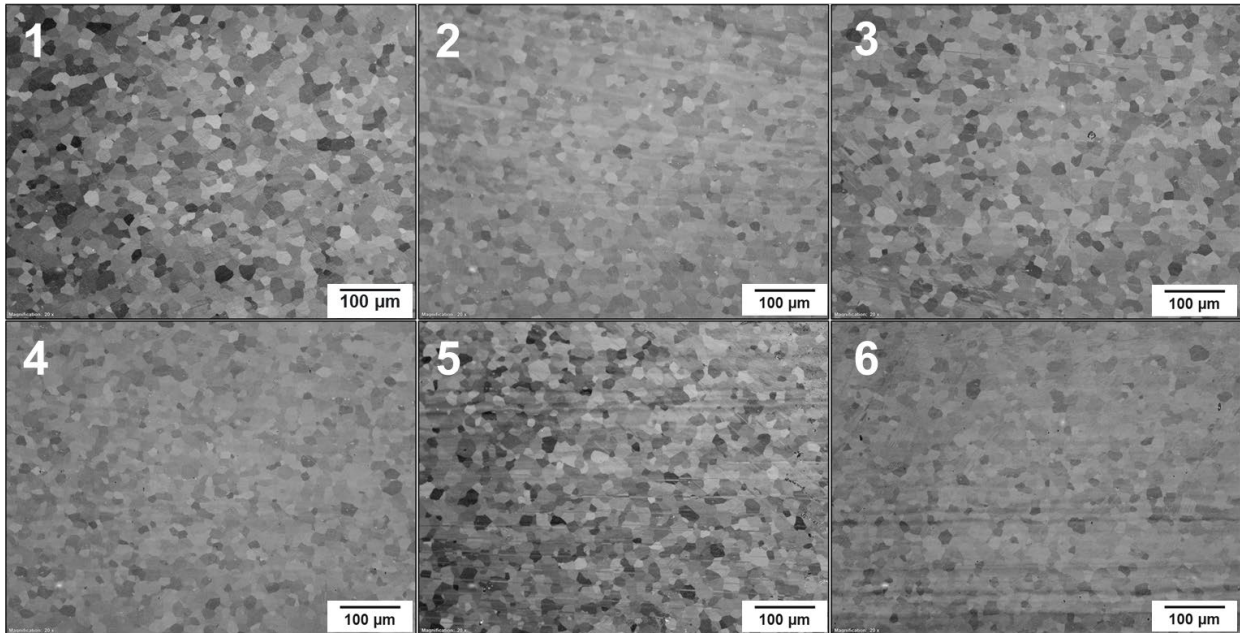
Figure 3-16. Optical micrograph of forged samples in conditions 1–6 after hot rolling to 0.04"
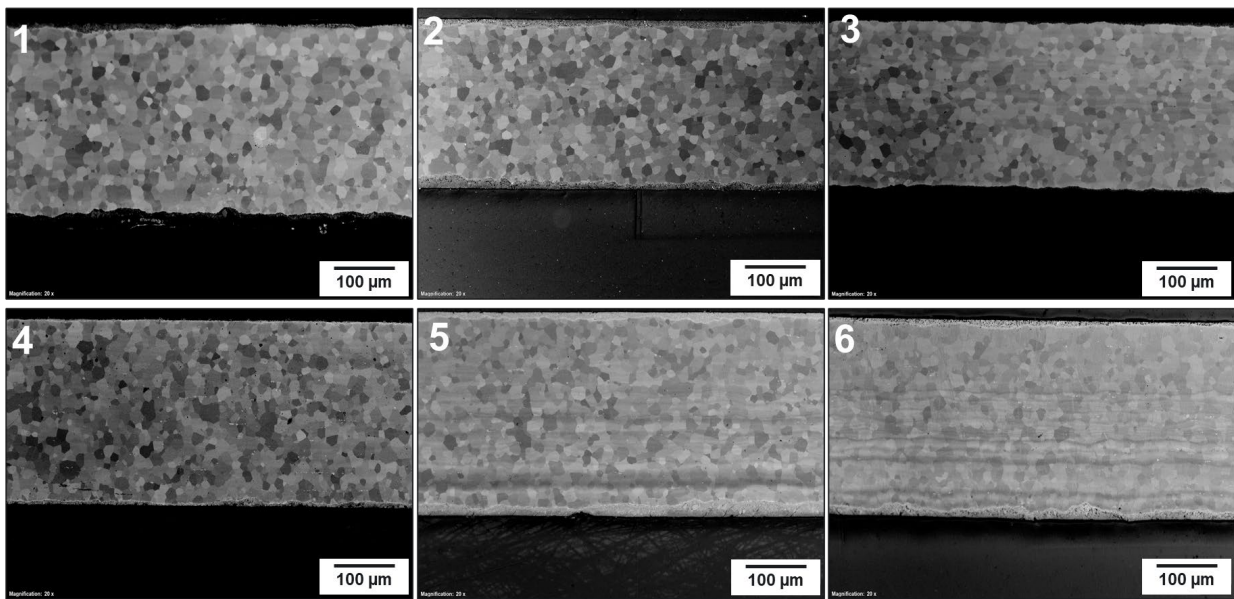and annealing. Images were taken at 20× magnification.

Figure 3-17. Optical micrographs of forged samples in conditions 1–6 after cold rolling to
0.0085" and annealing. Images were taken at 20× magnification.

Table 3.6. Average grain diameter after hot and cold rolling to 0.04" and 0.0085", respectively, then annealing

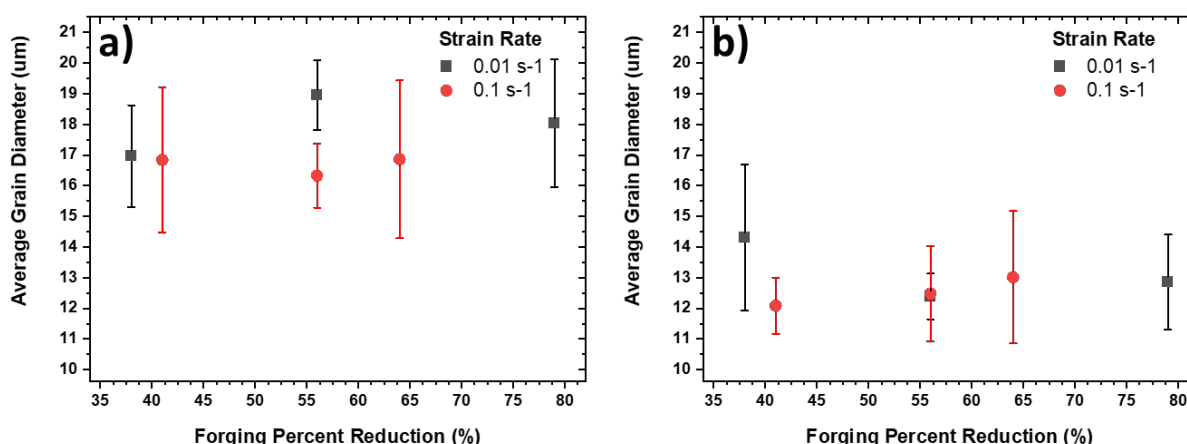| As-Forged Sample Number	Reduction Percentage	Strain Rate (s^{-1})	Average Grain Diameter	
			Hot Rolled to 0.04" and Annealed (µm)	Cold Rolled to 0.0085" and Annealed (µm)
1	79.4%	0.01	18 ± 2	13 ± 2
2	37.7%	0.01	17 ± 2	14 ± 2
3	56.1%	0.01	19 ± 1	12 ± 1
4	41.2%	0.10	17 ± 3	12 ± 1
5	555.8%	0.10	16 ± 1	12 ± 2
6	63.8%	0.10	17 ± 3	13 ± 2
		Average	17 ± 2	13 ± 2

Figure 3-18. Plots of the average grain sizes for Samples 1–6 (a) after hot rolling to 0.04" and annealing and (b) after cold rolling to 0.0085" and annealing. Error bars represent the standard deviation of the dataset.

Similar to the hot-rolled and annealed microstructure, the final cold-rolled and annealed microstructure showed a homogeneous grain size and was consistent across all six samples (Figure 3-17). However, cold rolling to the final foil thickness of 0.0085" and annealing (45 minutes at 700°C) produced a smaller average grain diameter (13 ± 2 µm vs. 17 ± 2). The average grain diameter and standard deviation for each of the forging conditions are displayed in Table 3.6 and Figure 3-18 alongside the results for hot-rolled samples. The average grain sizes for the cold-rolled, annealed samples fall into the size range typical for similarly prepared cold-rolled, annealed U-10Mo foils (W. E. Frazier et al. 2019; Kalsar et al. 2020; Saumyadeep Jana et al. 2017). To check for correlation between the starting, forged conditions and the final cold-rolled grain size, a Games-Howell pairwise comparison of the means was performed; it indicated no statistically significant difference in the mean grain size after final cold rolling and annealing across the six sample conditions.

As discussed in previous sections, it is important to emphasize that the sample size analyzed was small and thus too few data were collected to draw statistically significant conclusions

about the final grain size. However, our grain size results agree with data from previous U-10Mo studies (W. E. Frazier et al. 2019; Kalsar et al. 2020; Saumyadeep Jana et al. 2017).

3.3.2 Carbides and BSE Analysis

BSE images showing UC morphology for the hot-rolled and cold-rolled, annealed conditions are presented in Figure 3-19 and Figure 3-20. The UC particle size after hot rolling to 0.04" and annealing ranged from 0.002–17.6 μm^2, with an average of 0.21 ± 0.91 μm^2. The average area percentage of carbides across all six samples was ~1%. Data on the average UC particle size and area percentage for all forging conditions after rolling operations is summarized in Table 3.7. There was no significant difference in mean carbide size for the six samples after hot rolling and annealing.
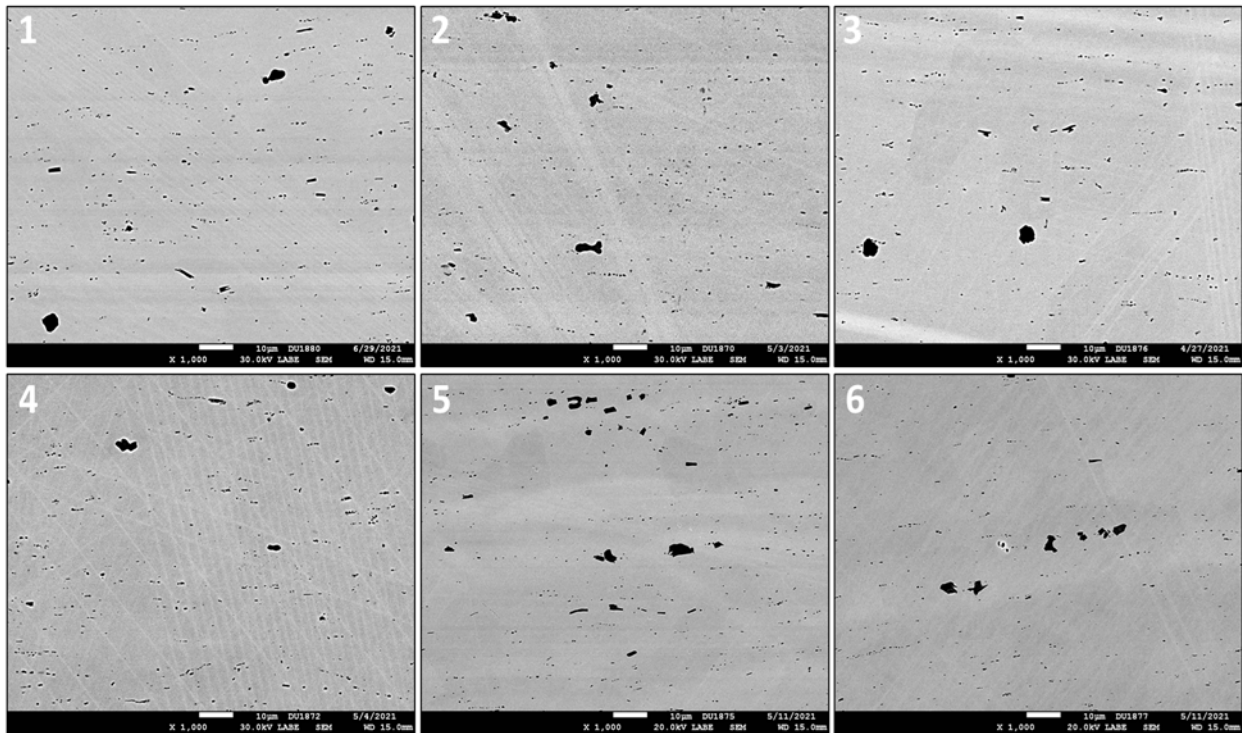

Figure 3-19. BSE images taken at 1000× magnification of Samples 1–6 after hot rolling to 0.04" and annealing
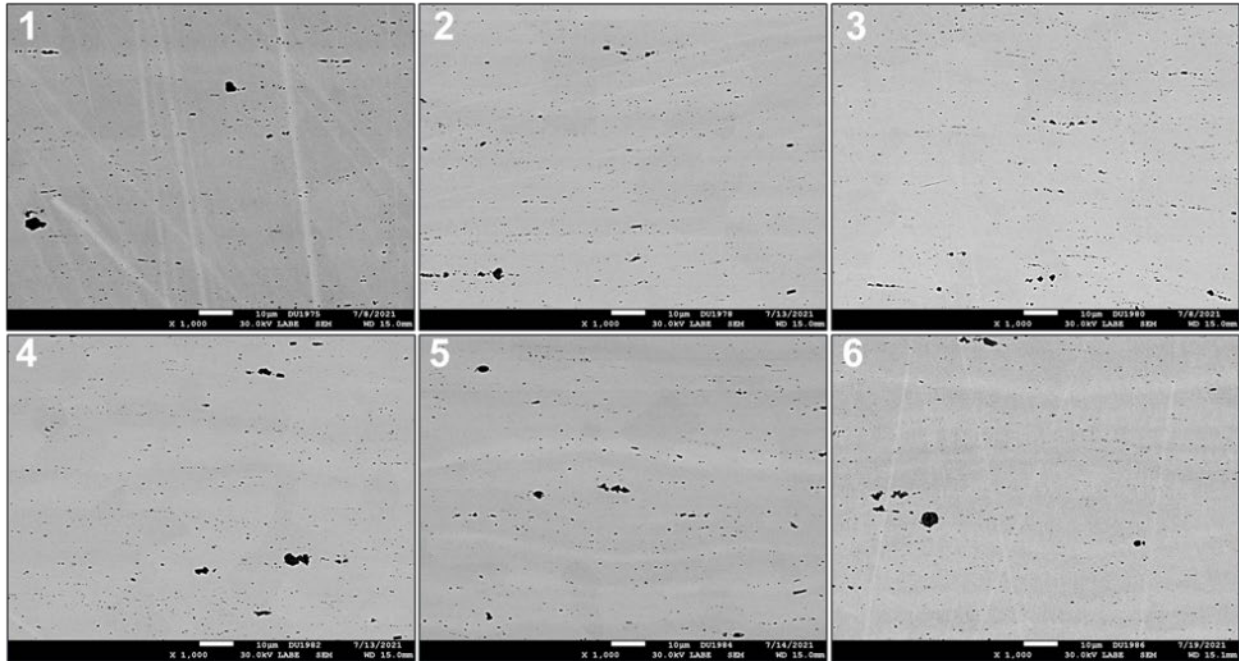
Figure 3-20. BSE images at 1000× magnification of Samples 1–6 after cold rolling to 0.0085"
and annealing

Table 3.7. Carbide size and area fraction after hot rolling to 0.04" and after cold rolling to
0.0085", then annealing

Sample #	Strain Rate (s^{-1})	Hot Rolled Annealed		Cold Rolled Annealed	
		Average UC Area Fraction (%)	Average UC Size (μm^2)	Average UC Area Fraction (%)	Average UC Size (μm^2)
1	0.01	1.15	0.24 ± 0.98	1.07	0.19 ± 0.72
2	0.01	1.18	0.17 ± 0.77	0.83	0.14 ± 0.38
3	0.01	1.06	0.24 ± 1.11	0.89	0.12 ± 0.21
4	0.10	1.05	0.20 ± 0.67	0.98	0.15 ± 0.78
5	0.10	1.37	0.26 ± 1.04	0.88	0.19 ± 0.51
6	0.10	0.84	0.19 ± 0.88	1.00	0.18 ± 0.91
	Average	1.11 ± 0.18	0.21 ± 0.91	0.94 ± 0.09	0.16 ± 0.62

After cold rolling and annealing, the average carbide size ranged from 0.002 to 18.0 μm^2, with an average of 0.16 ± 0.62 μm^2. There was no statistically significant difference among mean carbide sizes for the six samples in their final cold-rolled and annealed conditions. Therefore, regardless of the prior forging parameters such as strain rate and reduction percentage, the carbide size after final hot and cold rolling steps was approximately the same for all six samples.

As displayed in Figure 3-21 and Table 3.7, the average UC particle size after hot rolling appears to be slightly larger than that after final cold rolling to the 0.0085" foil thickness and annealing. A Games-Howell pairwise comparison of the means confirms a statistically significant difference. A possible explanation for this difference is that the larger UC particles fracturing during cold

rolling, increasing the concentration of smaller sized UC particles. This is observable when looking at the BSE images (Figure 3-19 and Figure 3-20), which contain a higher concentration of fine UC particles after cold rolling compared to after hot rolling. A histogram found in Figure A.10 under the appendix also shows an increase in the frequency of UC ranging from 0-0.15 μm^2 after cold rolling. The average area percentage of UC particles was similar after hot and cold rolling with an average of $1.1 \pm 1.11\%$ after hot rolling and annealing and $0.94 \pm 0.09\%$ after final cold rolling and annealing. Overall, the average UC particle size observed in the cold rolled and annealed condition is within the range seen in other studies of UC particles in U-10Mo (W. E. Frazier et al. 2019; Kalsar et al. 2020).
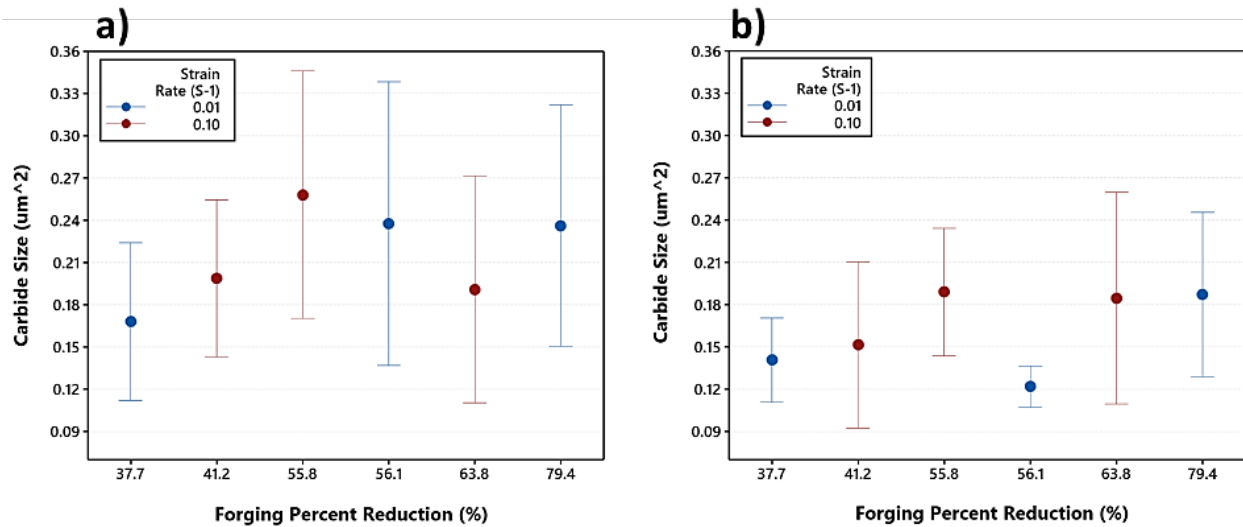

Figure 3-21. Plots of the average UC particle size (a) after hot rolling to 0.04" and annealing and (b) after cold rolling to 0.0085" and annealing, for all six forging conditions. Error bars represent the interval spread of the data at a 95% confidence interval. Horizontal access distributed evenly among six samples (values) and not to scale.

4.0 Conclusions

The purpose of this study was to understand the effects of hot forging before standard U-10Mo rolling operations. Implementing forging allowed for the use of a thick cast plate (~1" thick), which would otherwise be too thick to subject to rolling operations without first being cut into thinner sections. Information from this study also would be useful if forging is proposed as an additional hot working step for processing U10-Mo fuel foils. Six different forging conditions were applied after homogenization and before hot and cold rolling operations. The microstructure was analyzed at each stage of the U-10Mo processing and provided the following results:

- The cast Thick Plate 5 had low carbon content: 189 ± 21 ppm from bulk chemistry and 0.51 UC area percentage from BSE image analysis. The as-cast and the homogenized plates displayed microstructures typical in U-10Mo.

- Hot forging and annealing reduced the average grain size observed via OM from 833 ± 149 µm after homogenization to of 73 ± 60 µm after forging. Hot forging had no effect on molybdenum homogeneity, which was comparable to that in the homogenized condition (9.6 ± 0.2 wt% molybdenum).

- Forging produced a high density of dislocations along the grain boundaries, which later served as nucleation sites during annealing. The resulting annealed microstructure was heterogeneous, with smaller, strain-free grains surrounding large, deformed coarse grains. The average grain size (23–371 µm) and microstructure obtained from OM appeared to vary significantly with forging parameters. However, these variations did not appear to correlate with the reduction percentage or strain rate.

- EBSD results from as-forged Samples 1 and 2 showed that a greater forging reduction percentage resulted in faster recrystallization during the 1 h anneal at 700°C after forging. However, it did not appear to significantly affect the average grain size. The average grain size obtained from EBSD of as-forged Samples 1 and 2 was 16.3 ± 22.9 µm and 17.5 ± 42.4 µm, respectively. As-forged Sample 1 (79% reduction) was 40% recrystallized after annealing at 700°C for 1 h. As-forged Sample 2 (38% reduction) was 10% recrystallized after annealing at 700°C for 1 h.

- The initial forging conditions and resulting microstructure had no appreciable effect on the grain size after hot rolling or final cold rolling and annealing. Upon hot rolling to 0.04" and annealing, the average grain size for all six samples was approximately 17 ± 2 µm. After final cold rolling to 0.0085" and annealing, the average grain size was about 13 ± 2 µm for all six sample conditions.

- The average UC particle size appeared to decrease from the hot-rolled-and-annealed condition (0.21 ± 0.91 µm^2) to cold-rolled-and-annealed condition (0.16 ± 0.62 µm^2). This was attributed to fracture of larger UC particles during cold rolling operations.

5.0   Quality Assurance

This work was performed in accordance with the PNNL Nuclear Quality Assurance Program (NQAP). The NQAP complies with the United States Department of Energy Order 414.1D, *Quality Assurance*. The NQAP uses NQA-1-2012, *Quality Assurance Requirements for Nuclear Facility Applications* as its consensus standard and NQA-1-2012 Subpart 4.2.1, "Guidance on Graded Application of Nuclear Quality Assurance (NQA) Standard for Research and Development," as the basis for its graded approach to quality. This work emphasized acquiring new theoretical or experimental knowledge. The information associated with this report should not be used as design input or operating parameters without additional qualification.

6.0 References

Adam, K. F., Z. D. Long, and D .P. Field. 2017. "Analysis of Particle-Stimulated Nucleation (PSN)-Dominated Recrystallization for Hot-Rolled 7050 Aluminum Alloy." *Metallurgical and Materials Transactions A: Physical Metallurgy and Materials Science* 48 (4): 2062–2076. https://doi.org/10.1007/s11661-017-3967-3. https://link.springer.com/article/10.1007/s11661-017-3967-3.

Al-Qureshi, H. A., A. N. Klein, and M. C. Fredel. 2005. "Grain size and surface roughness effect on the instability strains in sheet metal stretching." *Journal of Materials Processing Technology* 170 (1-2): 204-210. https://doi.org/10.1016/j.jmatprotec.2005.04.116. https://www.sciencedirect.com/science/article/pii/S0924013605005443?via%3Dihub.

ASTM International. November 17 2021. *ASTM E112-13(2021), Standard Test Methods for Determining Average Grain Size.* West Conshohocken, PA.

Dziaszyk, S. , E. J. Payton, F. Friedel, V. Marx, and G. Eggeler. 2010. "On the characterization of recrystallized fraction using electron backscatter diffraction: A direct comparison to local hardness in an IF steel using nanoindentation." *Materials Science and Engineering: A - Structural Materials Properties Microstructure and Processing* 527 (29-30): 7854–7864. https://doi.org/10.1016/j.msea.2010.08.063. https://www.sciencedirect.com/science/article/pii/S0921509310009743.

Frazier, W. E., S. Hu, N. Overman, R. Prabhakaran, C. Lavender, and V. V. Joshi. 2019. "Recrystallization kinetics of cold-rolled U-10 wt% Mo." *Journal of Nuclear Materials* 513 (January 2019): 56-61. https://doi.org/10.1016/j.jnucmat.2018.10.046. https://www.sciencedirect.com/science/article/pii/S0022311518313631.

Frazier, William E., Shenyang Hu, Nicole Overman, Curt Lavender, and Vineet V. Joshi. 2018. "Short communication on Kinetics of grain growth and particle pinning in U-10 wt.% Mo." *Journal of Nuclear Materials* 498 (January 2018): 254-258. https://doi.org/10.1016/J.JNUCMAT.2017.10.041. https://www.sciencedirect.com/science/article/pii/S0022311517311170?via%3Dihub.

Hosford, William F. . 2010. *Physical Metallurgy*. Second ed.: CRC Press.

Hu, Xiaohua, Xiaowo Wang, Vineet V. Joshi, and Curt A. Lavender. 2018. "The effect of thermomechanical processing on second phase particle redistribution in U-10 wt%Mo." *Journal of Nuclear Materials* 500 (March 2018): 270-279. https://doi.org/10.1016/j.jnucmat.2017.12.042. https://www.sciencedirect.com/science/article/pii/S0022311517311091?via%3Dihub.

Huber, Z., M. Athon, S. V. Shen, E. Conte, K. McCoy, and C. Lavender. 2021. "Enhancing isotope mixing in U-10Mo downblend castings with electromagnetic stirring." *Journal of Nuclear Materials* 555 (153148). https://doi.org/10.1016/J.JNUCMAT.2021.153148. https://www.sciencedirect.com/science/article/pii/S0022311521003718.

Huber, Z., K. M. McCoy, M. Athon, I. Schwerdt, and C. Lavender. 2021. "Effects of casting parameters and impurity concentrations on as-cast U–10Mo." *Progress in Nuclear Energy* 140 (103921). https://doi.org/10.1016/j.pnucene.2021.103921. https://www.sciencedirect.com/science/article/pii/S014919702100281X.

Humphreys, F. J. , and M. Hatherly. 2004. *Recrystallization and Related Annealing Phenomena*. Second ed.: Elsevier Ltd.

INL. October 4 2018. *Specification for Low Enriched Uranium Monolithic Fuel Plates.* (Idaho Falls, ID: Idaho National Laboratory).

Jana, S. , A. L. Schemer-Kohrn, N. R. Overman, L. E. Sweet, E. J. Kautz, C. A. Lavender, and V. V. Joshi. 2019-01-31 2019. *Eutectoid Transformation in U10Mo Alloy: Effect of*

Deformation History and Homogenization Heat Treatment. (Richland, WA: Pacific Northwest National Laboratory). https://www.osti.gov/servlets/purl/1503687/.

Jana, Saumyadeep, Nicole Overman, Tamas Varga, Curt Lavender, and Vineet V. Joshi. 2017. "Phase transformation kinetics in rolled U-10 wt. % Mo foil: Effect of post-rolling heat treatment and prior γ-UMo grain size." *Journal of Nuclear Materials* 496 (December 2017): 215-226. https://doi.org/10.1016/j.jnucmat.2017.09.030. https://www.sciencedirect.com/science/article/pii/S0022311517309170.

Joshi, Vineet V., Eric A. Nyberg, Curt A. Lavender, Dean Paxton, and Douglas E. Burkes. 2015. "Thermomechanical process optimization of U-10wt% Mo – Part 2: The effect of homogenization on the mechanical properties and microstructure." *Journal of Nuclear Materials* 465 (October 2015): 710–718. https://doi.org/10.1016/J.JNUCMAT.2015.07.005. https://www.sciencedirect.com/science/article/pii/S002231151530091X.

Joshi, Vineet V., Eric A. Nyberg, Curt A. Lavender, Dean Paxton, Hamid Garmestani, and Douglas E. Burkes. 2015. "Thermomechanical process optimization of U-10 wt% Mo – Part 1: High-temperature compressive properties and microstructure." *Journal of Nuclear Materials* 465 (2015): 805–813. https://doi.org/10.1016/j.jnucmat.2013.10.065. https://www.sciencedirect.com/science/article/pii/S0022311517311091.

Jue, Jan-Fong, Tammy L. Trowbridge, Cynthia R. Breckenridge, Glenn A. Moore, Mitchell K. Meyer, and Dennis D. Keiser. 2015. "Effects of heat treatment on U–Mo fuel foils with a zirconium diffusion barrier." *Journal of Nuclear Materials* 460 (May 2015): 153-159. https://doi.org/10.1016/j.jnucmat.2015.02.017. https://www.sciencedirect.com/science/article/pii/S0022311515001129?via%3Dihub.

Kalsar, R., F. G . DeLemma, T. Trowbridge, E. L. Tegtmeier, R. McCabe, R. Prabhakaran, N. R. Overman, D. L. Blanchard, J. Schulthess, C. Brizzee, K. Bohn, J. Lopez, B. Alexander, C. Miller, N. J. Lombardo, and V. V. Joshi. August 31 2020. *Characterization Report for the MP-1 Experiment Fabrication Campaign.* Pacific Northwest National Laboratory (Richland, WA: Pacific Northwest National Laboratory). https://www.osti.gov/servlets/purl/1763443/.

Lee, P. S., H. R. Piehler, B. L. Adams, G. Jarvis, H. Hampel, and A. D. Rollett. 1998. "Influence of surface texture on orange peel in aluminum." *Journal of Materials Processing Technology* 80-81 (August 1998): 315–319. https://doi.org/10.1016/S0924-0136(98)00189-7. https://www.sciencedirect.com/science/article/pii/S0924013698001897?via%3Dihub.

Llewellyn, D. T. . 1998. *Steels: Metallurgy and Applications*. Third ed., edited by R.C. Hudd: Butterworth-Heinemann.

Llewellyn, D. T. , and R. C. Hudd. 1998. "Low-carbon strip steels." In *Steels* 1-136. Butterworth-Heinemann.

Pacheco, Robin Montoya, David John Alexander, Rodney James Mccabe, Kester Diederick Clark, Jeffrey E. Scott, Joel Dwayne Montalvo, and Pallas A. Papin. 2017. *Annealing of (DU-10Mo)-Zr Co-Rolled Foils* (Los Alamos, NM: Los Alamos National Laboratory). https://www.osti.gov/biblio/1340958-annealing-du-zr-co-rolled-foils.

Prabhakaran, R. , V. V. Joshi, M. A. Rhodes, A. L. Schemer-Kohrn, A. Guzman, and C. A. Lavender. March 2016. *U-10Mo Sample Preparation and Examination using Optical and Scanning Electron Microscopy.* (Richland, Washington: Pacific Northwest National Laboratory). https://www.pnnl.gov/main/publications/external/technical_reports/PNNL-25308Rev1.pdf.

Reeve, J. I., B. J. Schuessler, W. E. Frazier, D. P. Field, and V. V. Joshi. 2022. "The role of second phase particles and grain boundaries on recrystallization: Quasi-in situ experiments and modeling in U-10Mo alloy system." *Journal of Nuclear Materials* 559

(153445). https://doi.org/10.1016/j.jnucmat.2021.153445.
https://www.sciencedirect.com/science/article/pii/S0022311521006656?via%3Dihub.

Schuessler, B. J., D. P. Field, N. R. Overman, and V. V. Joshi. 2021. "The Effect of Homogenization Heat Treatment on the Texture Evolution in U-10Mo Alloy." *Metallurgical and Materials Transactions A-Physical Metallurgy and Materials Science* 52 (9): 3871-3879. https://doi.org/10.1007/s11661-021-06349-8. https://link.springer.com/article/10.1007/s11661-021-06349-8.

Sease, J. D. , R. T. I. Primm III, and J. H. Miller. September 2007. *Conceptual Process for the Manufacture of Low-Enriched Uranium/Molybdenum Fuel for the High Flux Isotope Reactor.* Oak Ridge National Laboratory, (Oak Ridge, TN). https://www.osti.gov/servlets/purl/921766-FRFuEo/.

Senor, D. J., and D. E. Burkes. 2014. *Fuel Fabrication Capability Research and Development Plan: Global Threat Reduction Initiative - Convert Program.* (Richland, Washington: Pacific Northwest National Laboratory). https://www.pnnl.gov/main/publications/external/technical_reports/PNNL-22528Rev1.pdf.

Wachs, Daniel M. , Curtis R. Clark, and Randall J. Dunavant. Feb 2008. *Conceptual Process Description for the Manufacture of Low-Enriched Uranium-Molybdenum Fuel.* (Idaho National Laboratory). https://inldigitallibrary.inl.gov/sites/sti/sti/4010771.pdf.

Wright, S. I., M. M. Nowell, and D. P. Field. 2011. "A Review of Strain Analysis Using Electron Backscatter Diffraction." *Microscopy and Microanalysis* 17 (3): 316–329. https://doi.org/10.1017/S1431927611000055. https://www.ncbi.nlm.nih.gov/pubmed/21418731.

Xu, Zhijie, Vineet Joshi, Shenyang Hu, Dean Paxton, Curt Lavender, and Douglas Burkes. 2016. "Modeling the homogenization kinetics of as-cast U-10wt% Mo alloys." *Journal of Nuclear Materials* 471 (April 2016): 154–164. https://doi.org/10.1016/j.jnucmat.2015.11.026. https://www.sciencedirect.com/science/article/pii/S002231151530.

Yamaguchi, K., and P. B. Mellor. 1976. "Thickness and grain size dependence of limit strains in sheet metal stretching." *International Journal of Mechanical Sciences* 18 (2): 85–90. https://doi.org/10.1016/0020-7403(76)90055-2. https://www.sciencedirect.com/science/article/pii/0020740376900552?via%3Dihub.
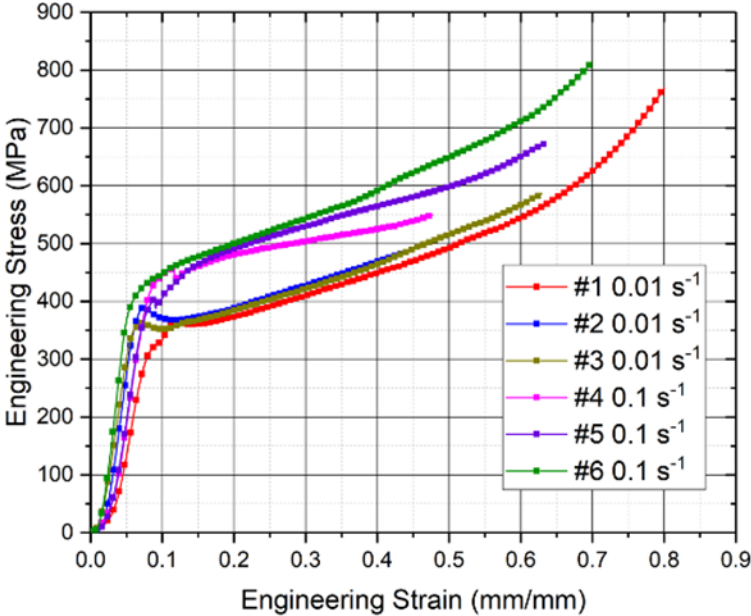
Appendix

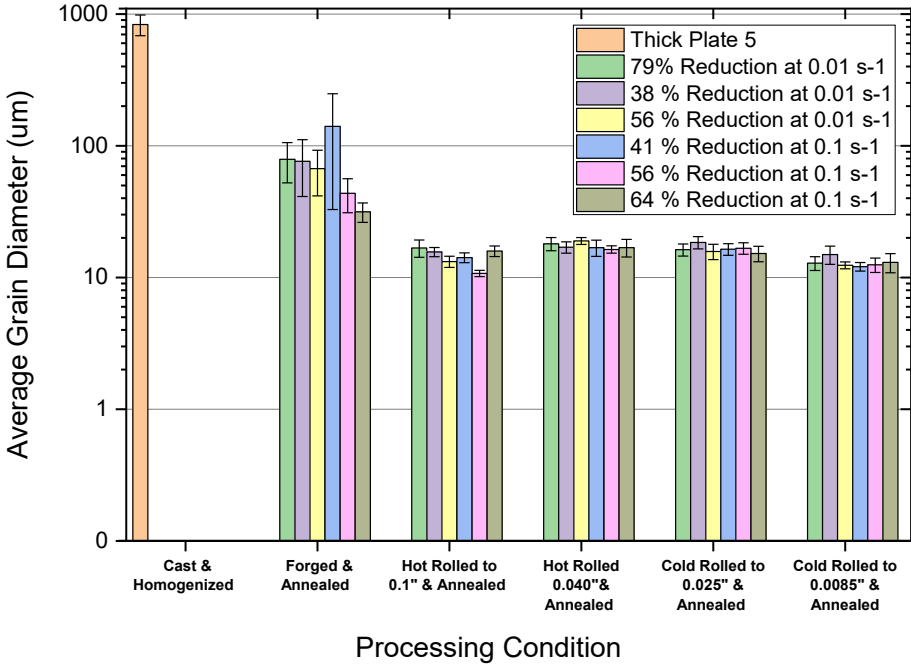Figure A.1. Stress-strain curves from the six different forging conditions

Figure A.2. Average grain size for the homogenized plate and the six forging reductions at five stages of thermomechanical processing (Forged annealed, hot rolled to 0.1" annealed, hot rolled to 0.04" annealed, cold rolled to 0.025" annealed, and cold rolled to 0.0085" annealed). Error bars represent plus or minus the standard
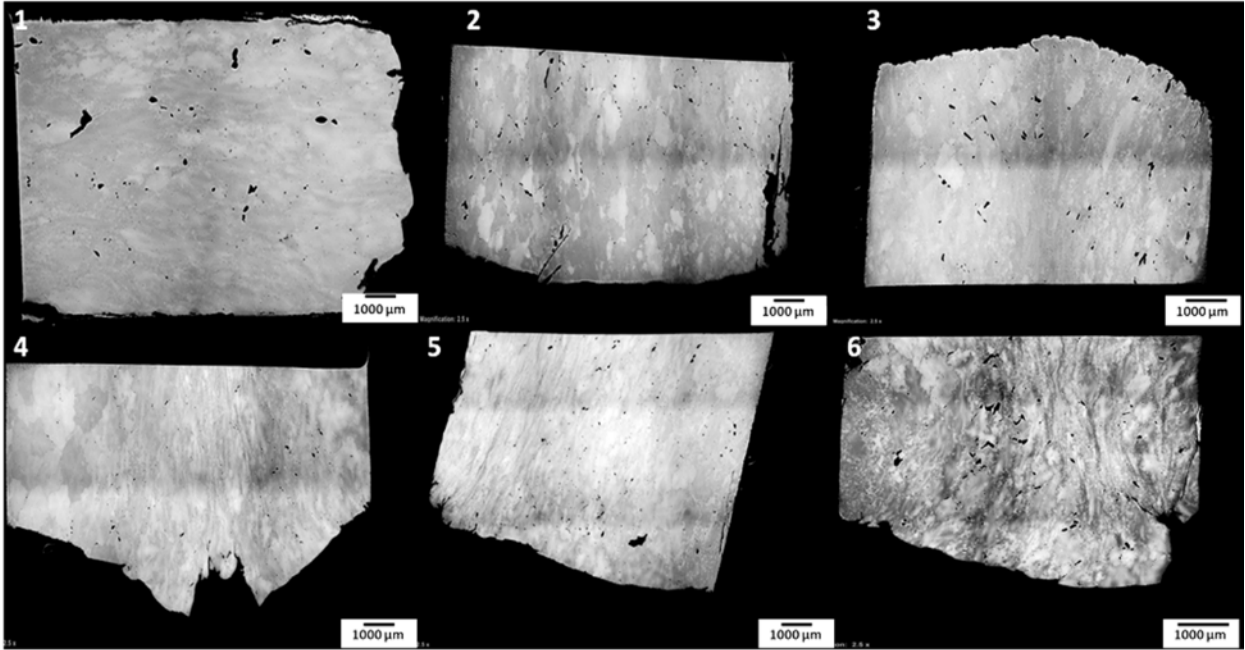
deviation of the dataset. Y axis scaled using $\log_{10}$.

Figure A.3. Montage images taken at 2.5× magnification of forged-and-annealed Samples 1–6
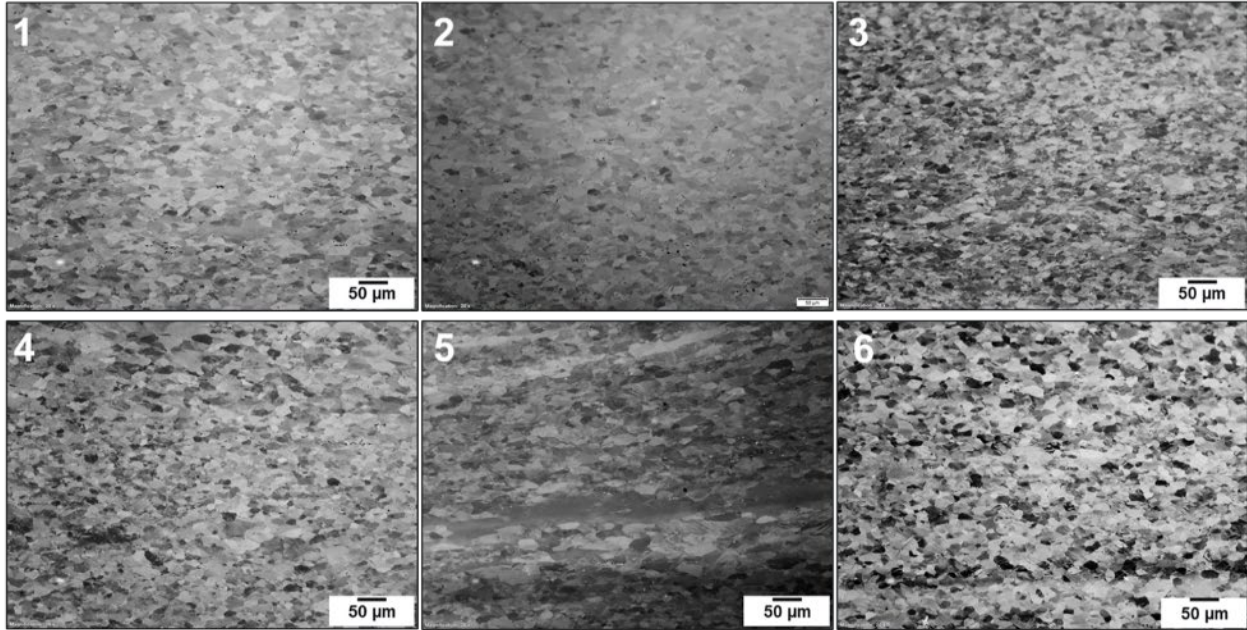
Figure A.4. Optical micrographs of forged Samples 1–6 after hot rolling to 0.1". Images were taken at 20× magnification.
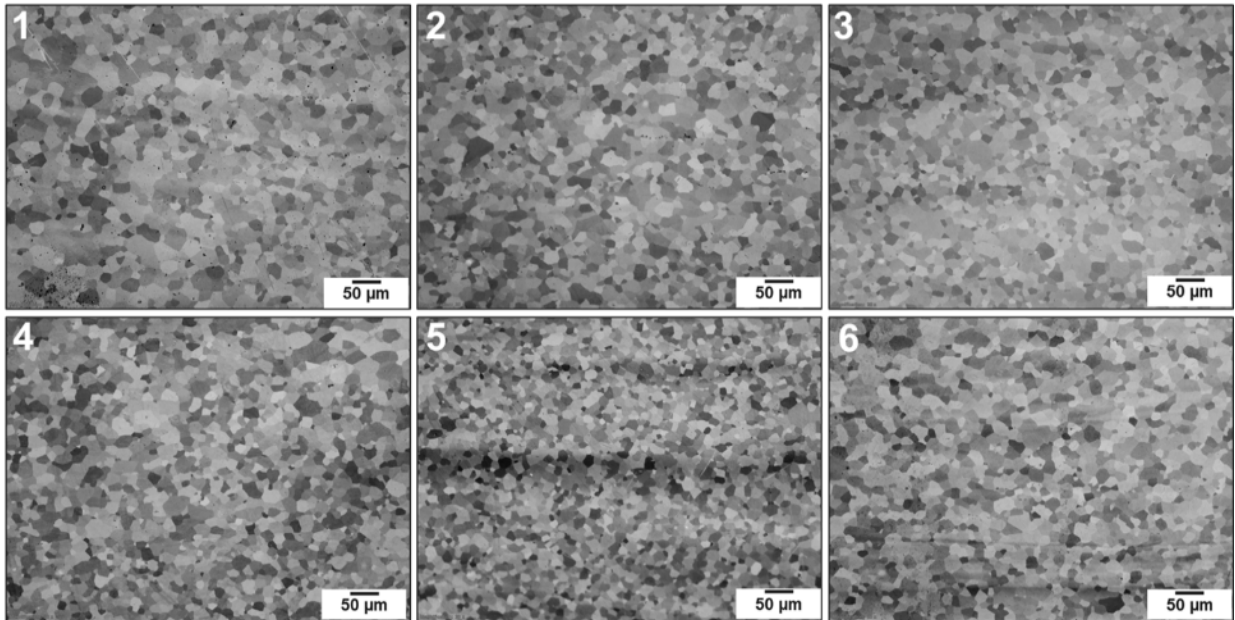
Figure A.5. Optical micrographs of forged Samples 1–6 after hot rolling to 0.1" and annealing. Images were taken at 20× magnification
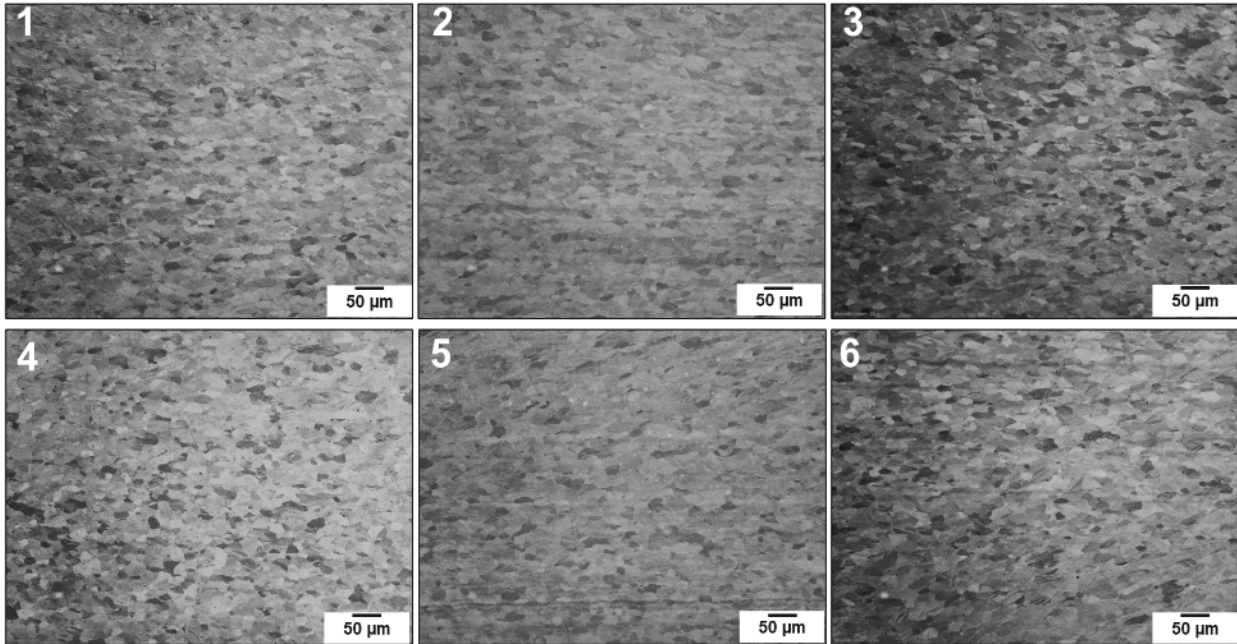
Figure A.6. Optical micrographs of forged Samples 1–6 after hot rolling to 0.04". Images were taken at 20× magnification.
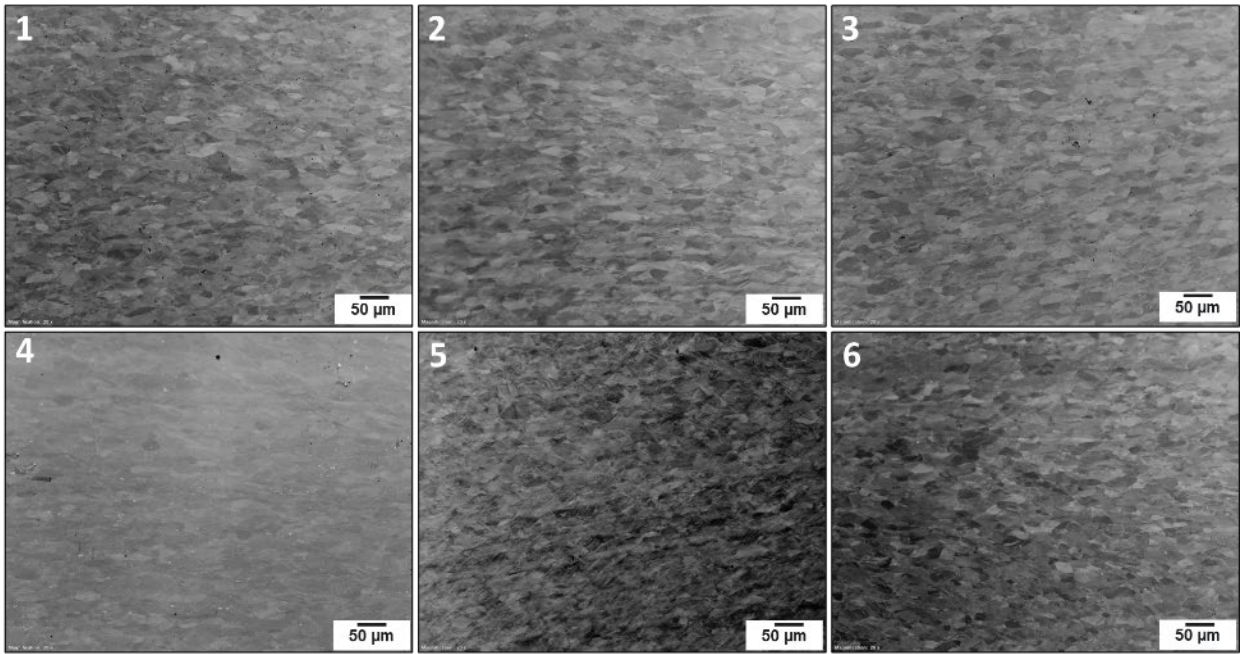

Figure A.7. Optical micrographs of forged Samples 1–6 after cold rolling to 0.025". Images were taken at 20× magnification.
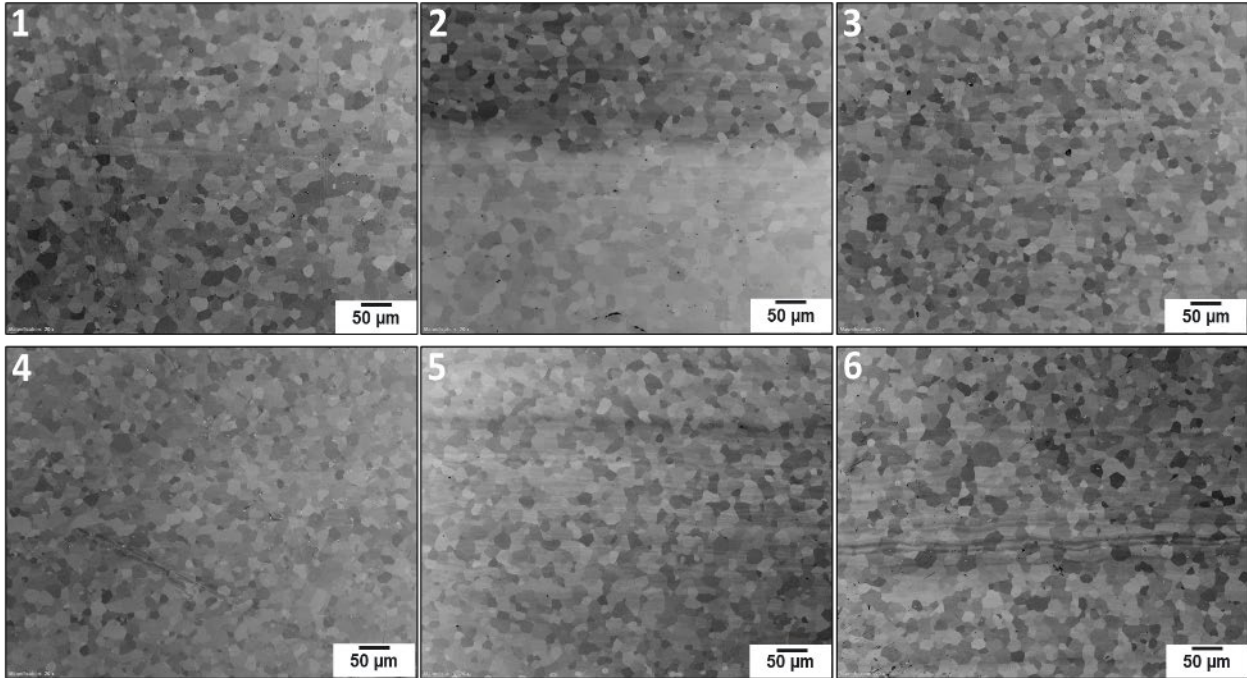
Figure A.8.Optical micrographs of forged Samples 1–6 after cold rolling to 0.025" and annealing. Images were taken at 20× magnification.
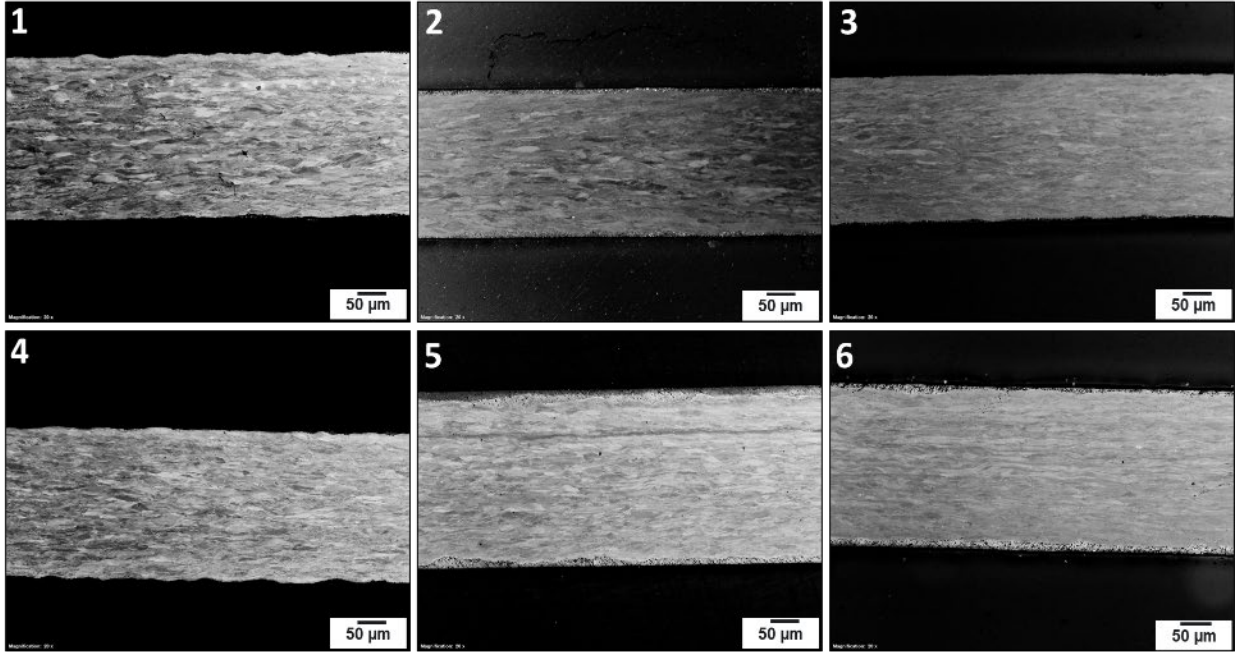
Figure A.9. Optical micrographs of forged Samples 1–6 after cold rolling to 0.0085". Images were taken at 20× magnification.
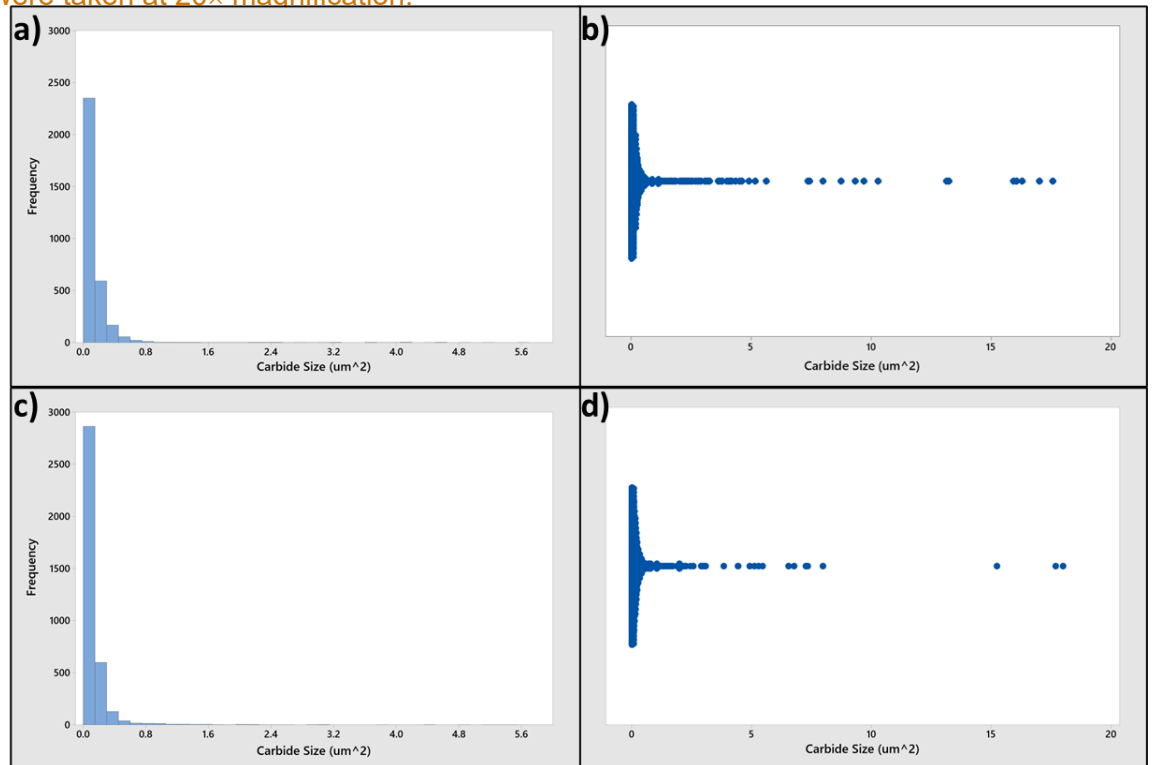

Figure A.10. Histograms and individual data plots after hot rolling and annealing (a, b) and cold rolling and annealing (c, d) for all 6 forged sample conditions. 3277 UC were examined after hot rolling and 3736 UC after cold rolling. Both histograms show right-skewed distributions with higher frequency of data among smaller values. After cold rolling there is a higher frequency of UC in the 0-0.15 μm^2 bin range. Histograms (a, c) only show data points up to 6 μm^2 due to infrequency of points beyond this size. The full data set is represented in the corresponding individual data plots (b, d).

Pacific Northwest
National Laboratory

902 Battelle Boulevard
P.O. Box 999
Richland, WA 99354
1-888-375-PNNL (7665)

www.pnnl.gov